

## Fast Dynamical Modelling of Milky Way Globular Clusters – I. Implications for Initial Cluster Densities

NOLAN DICKSON,<sup>1</sup> VINCENT HÉNAULT-BRUNET,<sup>1</sup> FOTIOS FRONIMOS POULIASIS,<sup>2</sup> MARK GIELES,<sup>2,3,4</sup> AND PETER J. SMITH<sup>5,6</sup>

<sup>1</sup>*Department of Astronomy and Physics, Saint Mary's University, 923 Robie Street, Halifax, NS B3H 3C3, Canada*

<sup>2</sup>*Institut de Ciències del Cosmos (ICCUB), Universitat de Barcelona (UB), c. Martí i Franqués, 1, 08028 Barcelona, Spain*

<sup>3</sup>*ICREA, Pg. Lluís Companys 23, E08010 Barcelona, Spain*

<sup>4</sup>*Institut d'Estudis Espacials de Catalunya (IEEC), Edifici RDIT, Campus UPC, 08860 Castelldefels (Barcelona), Spain*

<sup>5</sup>*Max Planck Institute for Astronomy, Königstuhl 17, D-69117 Heidelberg, Germany*

<sup>6</sup>*Department of Physics and Astronomy, University of Heidelberg, Im Neuenheimer Feld 226, D-69120 Heidelberg, Germany*

(Dated: Accepted XXX. Received YYY; in original form ZZZ)

### ABSTRACT

We infer the initial conditions of Milky Way (MW) globular clusters (GCs) from present-day observations, through the coupling of recently updated rapid cluster evolution models with multimass equilibrium models. This novel method is validated by fitting to simulated observations of a large grid of star-by-star Monte Carlo models, demonstrating that we are able to recover cluster properties like the total mass, half-mass radius/density and black hole (BH) mass fraction, both initially and at the present day, across a large region of parameter space. We apply this framework to a sample of 40 MW GCs, fitting to a suite of observed radial profiles of number densities, proper motions, line-of-sight velocities and stellar mass functions. From these fits we infer a distribution of initial half-mass densities with a median and  $1\sigma$  width, across our sample, of  $\rho_{h,0} = 10^{6.4\pm 0.9} M_{\odot} \text{pc}^{-3}$ , higher than what is found for young massive clusters in the Local Universe and in line with young clusters at high redshift. We also find stellar initial mass functions that are bottom-light in comparison to canonical prescriptions, and relatively small present-day BH mass fractions ( $\lesssim 1.5\%$ ). We discuss the implications of these initial cluster densities for observations of high-redshift proto-GCs, binary BH merger rates and intermediate-mass BHs (IMBHs) in GCs. Finally, we quantify how these densities may depend on assumptions typically made surrounding BH formation and natal kicks.

### 1. INTRODUCTION

Massive globular star clusters (GCs) provide an important fossil record for the study of large and small structures in the Universe, and are key for understanding a number of important cosmic processes such as star formation, galaxy assembly, black hole (BH) growth and gravitational waves (GWs).

Despite their importance, and ubiquity in galaxies like our own Milky Way (MW), the precise origins and initial conditions of the ancient GCs we see today remains a much studied, but inconclusive, question (see e.g. [D. A. Forbes et al. 2018](#); [J. M. D. Kruijssen 2026](#)). The formation and early evolution of clusters are essential to the progression of their entire lifetimes, and influence the possible growth of intermediate-mass BHs (IMBHs) (e.g. [S. F. Portegies Zwart & S. L. W. McMillan 2002](#); [M. S. Fujii et al. 2024](#)) and multiple populations ([N. Bastian & C. Lardo 2018](#)). However, we cannot easily observe these conditions directly, as nearby GCs are univer-

sally ancient systems, and differences with observed young massive clusters (YMCs) sow uncertainty about whether the young clusters in the local Universe will evolve one day into GCs as we see at the present day, or if clusters formed differently in the ancient Universe than today ([S. F. Portegies Zwart et al. 2010](#); [M. R. Krumholz et al. 2019](#)).

Modern high-resolution simulations of GC formation attempt to reproduce observed cluster populations through the inclusion of a number of physical processes, including star formation, stellar and binary evolution, and collisional dynamics, across a variety of interstellar environments (e.g. [C. Cournoyer-Cloutier et al. 2024](#); [B. Polak et al. 2024](#); [M. Reina-Campos et al. 2025](#); [N. Lahén et al. 2025b,a](#); [C. E. Williams et al. 2025](#)). However, the self-consistent modelling of cluster formation and evolution remains too computationally expensive to enable the exploration of large regions of possible parameter space.

In recent years, with the advent of JWST, observations of strongly gravitationally lensed galaxies have enabled the discovery of young and massive candidate proto-GCs at high redshifts (e.g. [E. Vanzella et al. 2023](#); [A. Claeysens et al.](#)

2023; A. Adamo et al. 2024; A. Claeysens et al. 2026). Though there remain significant uncertainties in the derivation of the physical properties of these systems, and it is still not entirely clear if these proto-GCs are destined to evolve into the MW-like GC populations we see today.

On the opposite end of cluster lifetimes, at the present-day, we have access to extensive observations of GCs within the MW from ground and space-based facilities (e.g. L. L. Watkins et al. 2015; S. Kamann et al. 2018; M. Libralato et al. 2022; Gaia Collaboration et al. 2023; M. Libralato et al. 2024). This data has enabled the detailed modelling of a large number of GCs through various approaches (e.g. A. Zocchi et al. 2019; V. Hénault-Brunet et al. 2019, 2020; N. Z. Rui et al. 2021a; E. Vitral et al. 2022, 2023). These efforts have been used to explore the structure, kinematics, chemistry, and stellar and remnant populations of these systems. Of particular note, many recent studies have explored the populations of BHs which may exist today within most GCs, through both direct observations (e.g. J. Strader et al. 2012; A. Paduano et al. 2024; B. Giesers et al. 2018, 2019; Gaia Collaboration et al. 2024; M. Whitaker et al. 2026), and indirect modelling (e.g. N. C. Weatherford et al. 2018, 2020; A. Askar et al. 2018).

In N. Dickson et al. (2023, 2024, hereafter D23; D24), we harnessed a variety of observational datasets in order to fit multimass equilibrium models to a large sample of the most well studied MW GCs. These models were used to infer the composition and distribution of luminous and dark mass within the clusters, and in particular to place constraints on their stellar initial mass functions (IMF) and BH populations, finding (alongside H. Baumgardt et al. 2023) a non-canonical, bottom-light IMF and relatively small (but typically non-zero) total BH masses.

These observations and models of MW clusters at the present day,  $\sim 12$  Gyr after their birth, represent a key boundary condition in our attempts to constrain the formation and long-term evolution of GCs. However, bridging this gap between the initial and current conditions of clusters is not straightforward, as the clusters undergo Gyrs of evolution driven by internal and external mechanisms impacting their mass loss and size evolution. Additionally, the evolution may be strongly impacted by a number of smaller-scale physical processes which remain uncertain, such as the stellar IMF, or the supernovae natal kicks received by BHs upon their formation (e.g. S. Popov et al. 2025).

The long-term dynamical evolution of GCs is driven by a tendency towards a state of unstable thermal equilibrium, and the corresponding flow of heat from the core to satisfy the energy demands of the system (M. Hénon 1961). This evolution is the emergent result of a number of physical processes, such as two-body relaxation, stellar evolution and evaporation in the tidal field of the host galaxy (L. S. Spitzer 1987;

D. Heggie & P. Hut 2003). A great deal of research has approached this complex evolution through direct  $N$ -body integration methods. However, this comes with significant computational costs, and only recently has it become possible to simulate clusters of  $> 10^6$  stars (e.g. L. Wang et al. 2016; M. Arca Sedda et al. 2024; P. Bianchini et al. 2026). M. Hénon (1971a,b) style Monte Carlo dynamical models, such as Cluster Monte Carlo (CMC; C. L. Rodriguez et al. 2022) and Monte Carlo Cluster Simulator (MOCCA; A. Hupki & M. Giersz 2013; M. Giersz et al. 2013), offer significantly lower computational costs and are used to simulate clusters of up to  $10^7$  stars (e.g. A. Mai et al. 2026). However, even with these faster methods, the computational costs are still so large that it is only possible to compute limited grids of large- $N$  models, and a complete exploration of realistic parameter space remains infeasible.

If we are willing to restrict our analysis to the bulk properties and overall stellar and remnant populations within a cluster, rather than examining the individual stars and remnants in detail, the fastest approach to modelling the dynamical evolution of GCs can be offered by semi-analytical models, with simple, physically motivated prescriptions describing the impacts of various relevant physical processes on cluster quantities like mass and radius over time.

M. Gieles et al. (2011) presented an expression for the evolution of the mass and size of a cluster within a tidal field based on the unification of the original models of Hénon for isolated (M. Hénon 1965) and tidally limited clusters (M. Hénon 1961). M. Hénon (1975) demonstrated that the heat flowing from the core of a cluster is controlled by the two-body relaxation demands of the rest of the system, while P. G. Breen & D. C. Heggie (2013) showed that this energy could be produced by a population of binary BHs (BBH), segregated to the core, through interactions causing the formation and hardening of the binaries, a process known as BH-burning. Based on these recipes, F. Antonini & M. Gieles (2020a,b); F. Antonini et al. (2023) developed the CLUSTERBH cluster evolution models, which self-consistently follow the evolution of both the cluster and its internal BH subsystem. Analogous models have also been constructed recently following similar prescriptions, such as EMACSS (P. E. R. Alexander & M. Gieles 2012; M. Gieles et al. 2014; P. E. R. Alexander et al. 2014), FASTCLUSTER (M. Mapelli et al. 2021) and RAPSTER (K. Kritos et al. 2024).

Recently, the CLUSTERBH models were expanded upon in F. Fronimos Pouliaxis et al. (2026, hereafter F26) to account for many other relevant physical processes, such as the effects of external tidal fields, a range of cluster metallicities, and different IMFs. These semi-analytical models were calibrated against a large grid of CMC cluster models (K. Kremer et al. 2020b), covering a range of initial conditions, and were able to reproduce the evolution of these star-by-star models

to within about 10 per cent, and their BBH merger rate to within about 20 per cent. The speed, flexibility and accuracy of these updated models provides a useful tool enabling the exploration of a number of open questions surrounding topics such as BH growth (D. Chattopadhyay et al. 2026, Marín Pina et al., in prep.), GW population synthesis (F. Fronimos Pouliaxis et al., in prep.), GC tidal streams (F. Fronimos Pouliaxis et al., in prep.) or, as we examine here, the initial conditions of GCs.

In this work, we combine these fast evolutionary models with the multimass equilibrium models previously used in D23; D24, allowing us to bridge the gap between the present-day observations and the unknown early conditions of a large sample of MW GCs. We infer in detail the distributions of stars and remnants in these clusters today by fitting on various observables, and working backwards through the clusters’ evolution, place constraints on their initial conditions.

In Section 2, we describe the evolutionary CLUSTERBH models, the multimass LIMEPY equilibrium models, and how they are coupled together, as well as the observational datasets and model-fitting procedures used. In Section 3, we test the ability of these models to reproduce the evolution of realistic clusters by fitting our models to simulated observations extracted from star-by-star dynamical models. Results for the fits to our MW cluster sample are then presented and discussed in Section 4, where we examine in more detail the inferred distributions of BH mass retained to the present day (Section 4.3), the stellar IMF (Section 4.4) and the cluster initial conditions (Section 4.5). Finally, in Section 5, we discuss the implications of our results on cluster formation, IMBH growth, and GW rates, before concluding in Section 6.

## 2. METHODS

### 2.1. CLUSTERBH Evolutionary Models

To model the bulk evolution of GCs and their BH subsystems from initial conditions to the present day, we use the latest version of the CLUSTERBH fast evolutionary models, as described in F26<sup>7</sup>.

In short, CLUSTERBH functions by considering the changes in the overall energy, total mass, mass in BHs and (through the assumption of virial equilibrium) half-mass radius of a cluster, as a result of a few major physical mechanisms, including two-body relaxation, stellar evolution and tidal evaporation to a host galaxy.

Two-body relaxation contributes to the cluster energy evolution after the formation of the first BBH in the cluster core, which we assume begins at the “core collapse time”  $t_{cc}$ , after which the energy production in the core and the energy

requirements of two-body relaxation in the rest of the cluster balance one another. The relaxation timescale, and thus the rate of change of the total cluster energy (excluding the negative energy locked in multiples), is itself related to the relative masses and radii of the stellar and BH populations within the cluster, and is thus dependent on the cluster metallicity and stellar IMF. The BH-burning process which generates the energy in the core of the cluster also results in ejections of BHs from the cluster. CLUSTERBH follows the prescriptions of P. G. Breen & D. C. Hoggie (2013) while in the balanced phase of evolution, but with an extra reduction to the BH ejection efficiency at later stages, to match the behaviour observed in  $N$ -body models.

Stellar evolution mass loss, through stellar winds and supernovae, contributes continuously to the expansion of the cluster over its lifetime, after some timescale  $t_{sev}$  marking the start of stellar evolution. It is most dominant at early times, as the most massive stars evolve and die. While CLUSTERBH is essentially a two-component model, consisting of BHs and all other non-BH objects, we note that the formation and retention of all non-BH stellar remnants are accounted for in the “stars” component and stellar-evolution driven mass loss mechanisms.

Finally, the presence of an external tidal field from a host galaxy like the MW causes the gradual evaporation of stars (preferentially low-mass) over the tidal boundary of the cluster. This tidal boundary is itself dependent on the strength of the external galactic potential, and thus the location of the cluster within the galaxy. In this work, we assume a static potential for the MW in the form of a singular isothermal sphere with a circular velocity of  $220 \text{ km s}^{-1}$ . An effective galactocentric radius for each cluster must be determined based on its orbit. This is discussed in more detail in Section 2.4.1.

F26 introduced 7 model parameters and a number of constants which define the various processes in CLUSTERBH, and calibrated the models through comparison with a large sample of CMC dynamical models (K. Kremer et al. 2020b; C. L. Rodriguez et al. 2022). In this work, we use the default values of each of these parameters, which correspond to the median best-fitting values found in F26 (see their Table 2).

### 2.2. Multimass LIMEPY Equilibrium Models

To model the present-day phase-space distribution of the GCs we use the LIMEPY multimass distribution-function (DF) based models (M. Gieles & A. Zocchi 2015), through the GCFIT Python package, as described in D23; D24<sup>8</sup>. The multimass version of these DF based models uses a set of discrete individual mass bins (described by the total ( $M_j$ ) and mean ( $m_j$ ) masses of each bin), representing a spectrum of stellar

<sup>7</sup> Available at <https://github.com/cBHBd/cBHBd>. Note that while CLUSTERBH is packaged alongside the BHB population synthesis models BHB-DYNAMICS, here CLUSTERBH is used in isolation.

<sup>8</sup> Available at <https://github.com/mgieles/limepy> and <https://github.com/nmdickson/GCfit>.

and remnant masses. The total DF is then defined as the sum of component DFs for each mass bin. These individual mass bins are required in order to account for important dynamical effects such as mass segregation, and to track specific types of objects, such as BHs.

The multimass models used here are defined by a number of free parameters, which dictate the physical solution of the LIMEPY DF. The central concentration of the model is defined by the (dimensionless) central potential parameter  $\hat{\phi}_0$ . The sharpness of the energy truncation near the tidal radius of the cluster, mimicking the effects of the host galaxy’s tides, is given by the parameter  $g$ , with lower values indicating a more abrupt truncation. For certain values of  $g$ , LIMEPY recovers some well-known families of models, such as the multimass King model (for  $g = 1$ ; R. W. Michie 1962; I. R. King 1966). The size and mass scales of the model are represented by the (present-day) total cluster mass  $M$  and 3D half-mass radius  $r_h$  parameters. The level of velocity anisotropy present in the model is dictated by the (dimensionless) anisotropy radius parameter  $\hat{r}_a$  (in units of the King radius  $r_0$ ), defining the radius at which the isotropic model core becomes radially anisotropic, before returning again to isotropy at the truncation radius.

The exact definition of  $\hat{\phi}_0$  and  $\hat{r}_a$  depends on the definition of the mean mass within LIMEPY, and, in contrast to D23; D24, here we choose to adopt the central mean mass, as defined in M. Gieles & A. Zocchi (2015), which we find to enable more stable computation of models containing many BHs<sup>9</sup>.

### 2.2.1. Updates to Energy Equipartition Prescriptions

Within the multimass version of the LIMEPY DF, the trend towards energy equipartition between objects of different masses, and the effects of mass segregation (M. Gieles & A. Zocchi 2015; M. Peuten et al. 2017; V. Hénault-Brunet et al. 2019), are captured by a mass-dependent velocity scale  $s_j$ , which is parametrized by the free parameter  $\delta$ , such that  $s_j^2 \propto m_j^{-2\delta}$ . Higher values of  $\delta$  represent increasingly mass segregated models, with  $\delta = 1/2$  representing a cluster that would be in equipartition in the limit  $\hat{\phi}_0 \rightarrow \infty$ .

However, this implies a shared equipartition relationship across all masses, including both stars and BHs. In reality, we expect BHs, which segregate very rapidly to form their own subsystem in the cluster core, to partly “decouple” from the rest of the stars. These central BHs should suppress the mass segregation of visible stars by dynamically heating the more massive stars and preventing their stratification to the core (E. Alessandrini et al. 2016; M. Peuten et al. 2017).

<sup>9</sup> It is straightforward to convert the values of  $\hat{\phi}_0$  and  $\hat{r}_a$  found under either the global or central mean mass definitions from one to the other, for comparison with other literature results, using equations 8 and 9 of M. Peuten et al. (2017).

However, a single shared equipartition parameter ( $\delta$ ) is unable to simultaneously capture both the segregation of BHs and the suppression of the equipartition among the rest of the stars at the same time. Therefore, in this work, we introduce a modified prescription for energy equipartition in LIMEPY.

To allow the BHs to partly decouple from the rest of the cluster, we instead compute the mass-dependent velocity scale parameter as:

$$s_j^2 \propto \begin{cases} m_j^{-2\delta}, & m_j < m_{\text{lim}} \\ \zeta m_j^{-2\delta}, & m_j \geq m_{\text{lim}} \end{cases} \quad (1)$$

where  $\zeta$  is a new free parameter, between 0 and 1, which allows the velocity scale to be reduced for all masses above a certain limiting value, which we take here to be  $m_{\text{lim}} = 3 M_\odot$ , to capture only the BHs. In tandem with this new prescription, we also now allow the anisotropy radius to be mass-dependent, by allowing the parameter  $\eta$  (such that  $r_{a,j} \propto r_a m_j^\eta$ ) to vary freely, whereas in D23 this was fixed to  $\eta = 0$ .

These changes allow the BHs in our models to be much more centrally concentrated, consistent with star-by-star GC models (e.g. P. G. Breen & D. C. Heggie 2013), and impacting the effects of the BH population on certain observable quantities, like the velocity dispersion.

### 2.3. Coupling CLUSTERBH and LIMEPY

The two models, CLUSTERBH (Section 2.1) and LIMEPY (Section 2.2), are coupled together in this work (hereafter referred to as cBH+limepy), allowing us to infer the initial conditions of real GCs from their present-day properties alone. To reflect this, in cBH+limepy the free parameters of total mass ( $M$ ) and half-mass radius ( $r_h$ ) are replaced with their initial (time 0) counterparts ( $M_0, r_{h,0}$ ).

The IMF, necessary to determine both the initial BH mass function (e.g. total and average BH mass) within CLUSTERBH and the present-day stellar and remnant mass bins within the multimass LIMEPY models, is implemented as a broken three-component power law, in keeping with the parametrization of canonical IMFs (e.g. P. Kroupa 2001). The three power-law slopes are given by the parameters  $\alpha_1, \alpha_2, \alpha_3$  (with break masses at 0.5 and 1  $M_\odot$  and bounded between 0.08 and 150  $M_\odot$ ). As there is increasing evidence that the low-mass IMF of MW GCs does not follow the commonly assumed P. Kroupa (2001) IMF (H. Baumgardt et al. 2023; N. Dickson et al. 2023), we wish to explore various IMFs with our models, and thus we let the  $\alpha_1$  and  $\alpha_2$  slopes vary freely.

These initial quantities are used to evolve, through clusterBH, the bulk quantities of the cluster over its lifetime, to its present-day age. The present-day total mass, half-mass radius and BH mass fraction are then used, alongside the other structural free parameters described in Section 2.2, to compute the multimass equilibrium LIMEPY DF based model. To

bridge the two models, we first determine from these quantities the present-day mass function (PDMF), which describes the mass bins in our multimass models, through a separate prescription. As described in D23, we do so using the mass function evolution algorithm implemented in the SSPTOOLS library<sup>10</sup>.

In short, this algorithm determines the number of stars which evolve off the main sequence over the lifetime of a cluster based on interpolated Dartmouth Stellar Evolution Program models (A. Dotter et al. 2007, 2008), and determines the types and masses of the resulting remnants based on their initial mass, metallicity and an initial-final mass relation (IFMR).

The white dwarf (WD) IFMR is interpolated from the MIST 2018 isochrones (A. Dotter 2016; J. Choi et al. 2016). All remnants with progenitor masses between the maximum WD progenitor mass and the minimum BH progenitor mass are assumed to be neutron stars (NS) with a mass of  $1.4 M_{\odot}$ . The BH IFMR is interpolated from a grid of stellar evolution library (SSE) models of different metallicities, using the updated version of SSE presented by S. Banerjee et al. (2020) and the rapid supernova scheme (C. L. Fryer et al. 2012). The effects of pair-instability supernovae and pulsational pair-instability supernovae are implemented according to the prescriptions of K. Belczynski et al. (2016).

As these remnants are formed, we mimic the effects of natal kicks causing the escape of these objects from the cluster by scaling the final number and mass of the created remnants by an “initial retention fraction”  $f_{\text{ret}}$ . For WDs, we assume  $f_{\text{ret}} = 100$  per cent. We assume a NS retention fraction of 10 per cent, as is common (e.g. E. Pfahl et al. 2002), though it has also been shown that the results of mass modelling are insensitive to the exact NS retention fraction due to the low total mass in NS (V. Hénault-Brunet et al. 2020).

The natal kicks of BHs are modelled in a more in-depth fashion to derive a value for  $f_{\text{ret}}$  as a function of the progenitor mass. By default, we follow a commonly assumed prescription, beginning by assuming the kick velocity is drawn from a Maxwellian distribution, with a dispersion of  $\sigma = (1 - f_b) 265 \text{ km s}^{-1}$ , where the base  $265 \text{ km s}^{-1}$  is the dispersion which has been found for NS (G. Hobbs et al. 2005)<sup>11</sup>, and  $f_b$  is the fallback fraction, the fraction of the stellar envelope which falls back onto the BH, which we interpolate from the same grid of SSE models as the BH IFMR. This fallback fraction is a function of both metallicity and stellar mass, and dictates how the kick velocity distribution varies, typically from full kicks at low BH masses to zero kicks at the highest masses, where BHs form without a super-

nova explosion (direct collapse; C. L. Fryer et al. 2012). We then compute the fraction of BHs retained in the cluster after the kicks by integrating this distribution up to the initial cluster central escape velocity, i.e. by evaluating the cumulative distribution function (CDF) of the Maxwellian at  $v_{\text{esc},0}$ :

$$f_{\text{ret}}(m_{\text{BH}}) = \text{erf}\left(\frac{v_{\text{esc},0}}{\sqrt{2}\sigma}\right) - \sqrt{\frac{2}{\pi}} \frac{v_{\text{esc},0}}{\sigma} \exp\left(\frac{-v_{\text{esc},0}^2}{2\sigma^2}\right) \quad (2)$$

where, as given above,  $\sigma$  is a function of the fallback fraction and the escape velocity is computed from the initial mass  $M_0$  and average half-mass density  $\rho_{\text{h},0}$  (as in F26):

$$v_{\text{esc},0} \approx 50 \text{ km s}^{-1} \left(\frac{M_0}{10^5 M_{\odot}}\right)^{1/3} \left(\frac{\rho_{\text{h},0}}{10^5 M_{\odot} \text{pc}^{-3}}\right)^{1/6}. \quad (3)$$

While this “canonical” prescription is commonly used, it is important to note that the true natal kick velocity distribution of BHs remains uncertain. Extensive modelling of BH formation and supernova explosions remains difficult and computationally expensive, while the limited examples of both direct and indirect observations of the effects of natal kicks on BHs provide an incomplete, and at times contradictory, measure of the distributions of velocities imparted by kicks (e.g. I. Mandel 2016; S. Repetto et al. 2017; P. Atri et al. 2019; S. Popov et al. 2025; R. Willcox et al. 2025a,b). Even within the commonly used setup of fallback-modulated Maxwellian BH kick distributions, the exact details of the chosen supernova engine can result in different expected fallback fraction curves, for example between the rapid and delayed convection mechanisms of C. L. Fryer et al. (2012).

Our flexible population synthesis models allow for variations in the magnitude and shape of kick distributions, which may have important implications on the required initial conditions of clusters. The potential impacts of different BH natal kick assumptions and IFMRs are discussed briefly in Section 5.6 and will be explored in more detail in a forthcoming work, while in this paper we adopt the above canonical prescriptions.

The binned BH mass function resulting from the creation of all BHs that will form from a given IMF and be initially retained in the cluster after natal kicks is also used by CLUSTERBH to determine the initial BH mass fraction and track the mean BH mass over time.

In contrast to D23; D24, the extra temporal information available from CLUSTERBH also allows us to account for and normalize the escape rates of stars and BHs within SSPTOOLS. To simulate the dynamical ejections of BHs over time from the cores of GCs, BHs are removed beginning from the heaviest mass bins (with larger gravitational interaction cross-sections) through to the lightest (e.g. M. Morscher et al. 2015; F. Antonini & M. Gieles 2020a), until the total BH mass fraction over time  $f_{\text{BH}}(t)$  matches that of the CLUSTERBH model.

<sup>10</sup> Available at <https://github.com/SMU-clusters/ssptools>.

<sup>11</sup> Although see also P. Disberg & I. Mandel (2025).

While in D23; D24 we were only able to allow the final BH retention fraction to vary freely, the coupling with the evolutionary models now provides more realistic, self-consistent constraints on the possible dynamical retention history of the BH populations.

The loss of stars, including all non-BH remnants, through dynamical ejections and tidal evaporation is modelled by assuming that the rate of change of the mass function over time goes as

$$\dot{f}(t, m) = -C(t)f(m)h(m), \quad (4)$$

where  $f(m)$  is the mass function (number of stars) at a given mass  $m$ ,  $C(t)$  is the normalization factor and  $h(m)$  is a function which accounts for the preferential loss of low-mass stars within the balanced evolution phase (E. Balbinot & M. Gieles 2018), such that

$$h(m) = \begin{cases} 1 - \left(\frac{m}{m_d}\right)^{1/2} & , m < m_d \\ 0 & , m > m_d \end{cases} \quad (5)$$

where  $m_d$  is the depletion mass, which we fix at  $1.2 M_\odot$ , based on the typical results of H. J. G. L. M. Lamers et al. (2013). Typically, determining the normalization factor, which is set by the total stellar mass loss rate, is non-trivial; however this information is readily available from CLUSTERBH, allowing us to compute  $C(t)$  directly:

$$C(t) = \frac{\dot{M}_*(t)}{\sum_j J_j} \quad (6)$$

where  $\dot{M}_*(t)$  is the stellar escape rate from CLUSTERBH, and  $J_j$  is the integration over  $mf(m)h(m)$  in each mass bin  $j$ , such that the mass loss rate in each bin is  $\dot{M}_j = -CJ_j$ . In D23; D24, this unknown quantity was simply set to  $\dot{M}_* = 0$ , meaning that the inferred IMF slopes effectively represented the PDMF, rather than the true IMF. In this work, however, this extra step in the modelling means we are able to directly infer the actual IMF slopes.

#### 2.4. Fitting of cBH+limepy Models

In this work, we use the models described in Section 2.3 to fit the observational data available for a large sample of MW GCs and explore their initial conditions.

##### 2.4.1. Cluster Data

For this analysis we return to the same sample of clusters chosen in D23; D24, which were selected to provide a large sample of MW GCs with sufficient quantity and quality of kinematic and stellar mass function data.

While this sample of 40 MW clusters allows us to survey the conditions of a significant population of the MW GCs, it should be noted, as discussed in D24, that the clusters chosen

are, by virtue of the required data quality, biased slightly towards more nearby, massive, and denser clusters.

The observational datasets used for each cluster are also the same as those used in D23; D24 (with a few small additions), and are briefly summarised below.

Binned radial profiles of proper motion (PM) dispersion, in both the radial and tangential directions, are provided by *Gaia* (Gaia Collaboration et al. 2023; D23) in the cluster outskirts and by the Hubble Space Telescope (*HST*; L. L. Watkins et al. 2015; M. Libralato et al. 2022) in the cores of most clusters in our sample. We also include the new PM dispersion profiles of  $\omega$  Cen from M. Häberle et al. (2025). Line-of-sight (LOS) velocity dispersion profiles are taken from compilations of various ground-based (N. Lützgendorf et al. 2013; H. Baumgardt & M. Hilker 2018; S. Kamann et al. 2018; H. Dalglish et al. 2020) and *Gaia* (H. Baumgardt et al. 2019) datasets. Projected number density profiles for most clusters are taken from T. J. L. de Boer et al. (2019), who combined *Gaia* star counts in the outskirts and *HST* counts (P. Miocchi et al. 2013) or ground-based surface-brightness profiles (SBPs, S. C. Trager et al. 1995) in the central regions. Three of our clusters (NGC 4372, NGC 4833 and NGC 5927) do not appear in this catalogue, and instead the surface brightness profiles compiled by H. Baumgardt (2017), based on data from J. Melbourne et al. (2000); A. Sarajedini et al. (2007); N. Kacharov et al. (2014) are used<sup>12</sup>. Finally, present-day local stellar mass functions are taken from H. Baumgardt et al. (2023), and consist of star counts extracted from a large number of *HST* pointings in each cluster.

The metallicities of the clusters are taken from W. E. Harris (1996). The ages of most clusters are taken from the catalogue of D. A. VandenBerg et al. (2013). Four clusters not in this catalogue instead have their ages taken from F. De Angeli et al. (2005, NGC 4372, NGC 6266) and A. Marín-Franch et al. (2009, NGC 5139, NGC 6093). However, our results are relatively insensitive to the exact ages chosen, except in cases where the clusters are actively dissolving, which do not appear in our chosen sample.

As discussed in Section 2.1, each cluster must also be placed on a circular orbit in CLUSTERBH. The galactocentric radius of this orbit is held constant throughout the evolution; however, in reality, the true orbit of clusters may be notably eccentric. In order to account for this, we follow the prescription described by H. Baumgardt & J. Makino (2003); P. E. R. Alexander et al. (2014) to compute an “effective circular orbit” at the galactocentric radius:

$$R'_G = R_a(1 - e) = \frac{2R_aR_p}{R_a + R_p} \quad (7)$$

<sup>12</sup> These three clusters were excluded from D23 due to the lack of number density data, but are now included in this study. All other clusters in our sample were present in D23.

where  $R_a$  and  $R_p$  are the apocentre and pericentre of a cluster’s orbit, taken from E. Vasiliev & H. Baumgardt (2021), and  $e$  is the orbital eccentricity. Placing clusters on this circular orbit roughly matches the tidal effects of the true eccentric orbits over the lifetime of the cluster (H. Baumgardt & J. Makino 2003; M. X. Cai et al. 2016).

#### 2.4.2. Fitting Procedure

In order to infer the posterior probability distributions of the model parameters that best describe each cluster, we utilize the same Bayesian parameter estimation methods as in D23. In particular, the cBH+limepy models are constrained by the datasets described above and the posterior is sampled using dynamic nested sampling (by the dynesty software package J. S. Speagle 2020), through the GCfit fitting pipeline. The free parameters inferred in this work are listed in Table 1 along with the adopted priors. In the same fashion as D23, we adopt, for most parameters, a uniform prior with limits chosen to bound a wide enough range of parameter space to be largely uninformative, or to cover the valid physical range of the parameter. For the heliocentric distance  $d$ , we instead adopt a Gaussian prior, with a mean and width taken from the averaged distances computed by H. Baumgardt & E. Vasiliev (2021).

Finally, to place some constraints on the expected relationship between the cluster core sizes and BH subsystems, which may not be discernible in the given observational data alone, we also include a regularization prior on the size of the cluster cores ( $r_c$ ). By examining the full grid of CMC models, a clear relationship emerges between  $r_c$  and the total mass in BHs (K. Kremer et al. 2025). We thus fit a linear relation between  $f_{\text{BH}}$  and  $\log(r_c/r_h)$  (using the “theoretical” core radius from S. Casertano & P. Hut 1985) in the CMC models, finding a slope, intercept and scatter of approximately 0.5, -0.5 and 0.2 respectively, and include a Gaussian, informative prior probability term centred on this relation to the posterior. However, tests without this extra constraint reveal that it does not typically have a large impact on the results presented here, with only a handful of core-collapsed clusters (discussed in Section 4.1) straying from the expected relation.

### 3. VALIDATION

To test the ability of our cBH+limepy models to reproduce the evolution of realistic clusters and recover their initial conditions, we first apply this fitting method to simulated present-day observations of star-by-star dynamical models, namely the existing grid of CMC models presented in K. Kremer et al. (2020b)<sup>13</sup>.

Simulations are selected from the available catalogue to cover a wide range of realistic MW GC conditions. To this

Parameter	Description	Prior
$\hat{\phi}_0$	Dimensionless central potential	$\mathcal{U}(0.0, 100.0)$
$g$	Truncation parameter	$\mathcal{U}(0.0, 3.5)^*$
$\log(\hat{r}_a)$	Dimensionless anisotropy radius	$\mathcal{U}(-2.0, 8.0)$
$\delta$	Velocity-scale mass dependence	$\mathcal{U}(0.1, 0.5)$
$\zeta$	Velocity-scale high-mass scaling	$\mathcal{U}(0.01, 1.0)$
$\eta$	Anisotropy-scale mass dependence	$\mathcal{U}(-5.0, 5.0)$
$M_0$	Initial total cluster mass [ $10^6 M_\odot$ ]	$\mathcal{U}(0.01, 5.0)$
$r_{h,0}$	Initial half-mass radius [pc]	$\mathcal{U}(0.01, 10.0)$
$\alpha_1$	IMF exponent ( $0.1 M_\odot < m \leq 0.5 M_\odot$ )	$\mathcal{U}(-1.0, 4.0)^*$
$\alpha_2$	IMF exponent ( $0.5 M_\odot < m \leq 1 M_\odot$ )	$\mathcal{U}(-1.0, \alpha_1)^*$
$F$	Mass function nuisance parameter	$\mathcal{U}(1.0, 5.0)$
$s^2$	Number density nuisance parameter	$\mathcal{U}(0.0, 15.0)$
$d$	Heliocentric distance [kpc]	$\mathcal{N}(d_{\text{lit}}, \delta d_{\text{lit}})$

**Table 1.** List of all free parameters, their descriptions and the prior probability distributions adopted here. The first six are structural LIMEPY parameters, the next four define the initial cluster conditions, and the final three parameters aid in comparing models to observations. Uniform priors ( $\mathcal{U}$ ) are indicated alongside their upper and lower bounds, while the prior on the distance is a Gaussian distribution ( $\mathcal{N}$ ) with mean  $d_{\text{lit}}$  and width  $\delta d_{\text{lit}}$  taken from H. Baumgardt & E. Vasiliev (2021). Prior bounds motivated by physical or model constraints are denoted by an asterisk. All others are chosen to bound a large enough area of parameter space to be largely uninformative. We note that the upper bound on the  $M_0$  prior is increased to  $20 \times 10^6 M_\odot$  for the massive clusters NGC 104 and NGC 5139.

end, we select all low-metallicity ( $Z = 0.0002, 0.002$ ) models in the catalogue (except for the smallest;  $N_0 = [2, 4] \times 10^5$ ), as well as eight of the higher-metallicity clusters ( $Z = 0.02$ ; spanning the available initial radii for  $N_0 = [8, 16, 32] \times 10^5$  models at  $R_G = 8$  kpc). Five of these selected models were subsequently excluded from our sample due to being either tidally disrupted before the end of the simulation, or being terminated early due to “collisional runaway” effects (see K. Kremer et al. 2020b for details). This yields a final sample of 53 CMC models. For each model we choose the final snapshot

<sup>13</sup> Available at <https://cmc.ciera.northwestern.edu>

in the catalogue to represent the present-day conditions of the mock clusters, resulting in a final age of around 13 Gyr for all clusters.

These models, which have circular galactic orbits with galactocentric distances of  $R_G = 20, 8$  and  $2$  kpc, are placed at heliocentric distances of  $8, 6.1$  and  $5$  kpc, typical of the distances seen in our sample of MW clusters. We then utilize the `CMCTOOLKIT` library (N. Z. Rui et al. 2021a,b) to compute projected positions, velocities and simulated photometry for stars in each snapshot. From these, we extract synthetic observations from each selected snapshot, designed to emulate the real observational datasets described in Section 2.4.1. For more details on the generation of these mock observations, see section 3.1 of D24.

We then fit the `cbh+limepy` models to these mock observations using the same priors as for the real clusters. The width of the distance prior is set to  $\sigma = 0.1$  kpc, to mimic realistic uncertainties. The fitting proceeds exactly as done when fitting on real clusters, with no information about the true evolutionary history of the models provided.

### 3.1. Results of Fits to Mocks

Figures 1 and 2 show an example of the resulting fits of our models to these mock observational datasets, for the CMC simulation with initial conditions  $N_0 = 8 \times 10^5$ ,  $r_{v,0} = 2$  pc,  $R_G = 2$  kpc,  $Z = 0.0002$  (corresponding to model number 75 in K. Kremer et al. 2020b). Figure 3 shows the recovery of the evolution over time of the bulk quantities of this same simulation. In Figure 4 we show the comparison between the true CMC values and our inferred values, for both the initial and present-day mass, radius, density and BH mass fraction, for the full sample of mocks we have examined. Our model fitting is able to successfully reproduce all of the simulated present-day kinematic, number density and mass function datasets, for all of the CMC models in our sample<sup>14</sup>. When comparing the inferred evolution of our models over time against the available snapshots of the CMC models, we see that despite fitting only to the present-day observables, we generally recover the evolution and initial conditions very well in most clusters.

It is clear from these figures that we are able to recover the present-day conditions of the entire mock cluster sample very well, where these quantities are directly constrained by the observational data. At most, we recover the mass, radius, density and BH mass fraction to within  $10^5 M_\odot$ ,  $1$  pc,  $0.25$  dex and  $1\%$  respectively, with the majority of clusters performing better than this. A handful of models with very low present-day values of  $f_{\text{BH}}$  are overestimated more significantly, however these correspond to models with almost

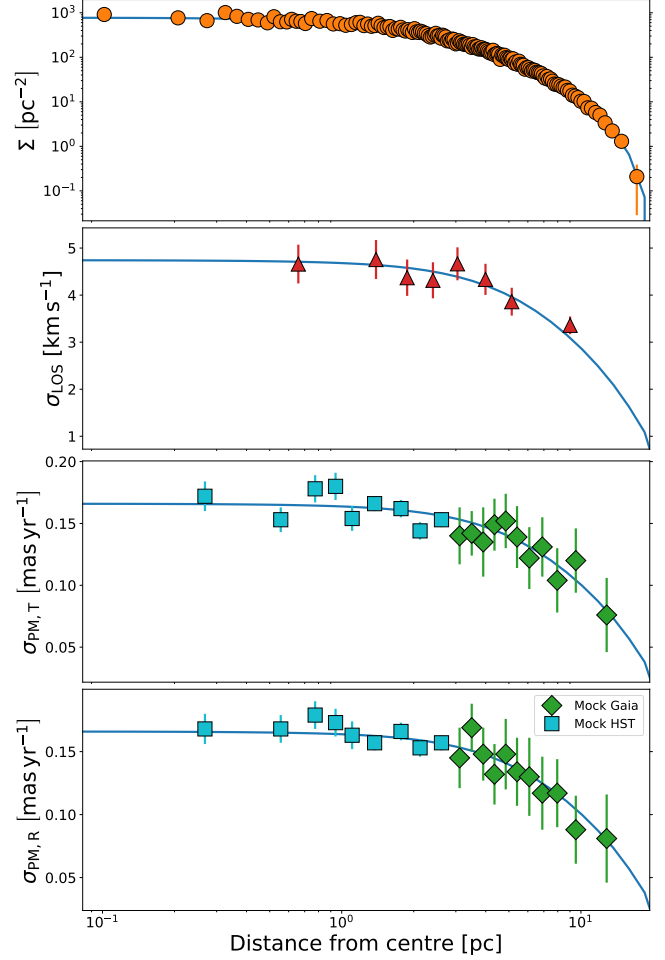


**Figure 1.** Model radial profiles (blue contours) of surface number density ( $\Sigma$ ), line-of-sight velocity dispersions ( $\sigma_{\text{LOS}}$ ), radial ( $\sigma_{\text{PM,R}}$ ) and tangential ( $\sigma_{\text{PM,T}}$ ) proper motion dispersions, for the fit of the mock observations of the CMC simulation with initial conditions  $N_0 = 8 \times 10^5$ ,  $r_{v,0} = 2$  pc,  $R_G = 2$  kpc and  $Z = 0.0002$ . The dark and light shaded regions represent the  $1\sigma$  and  $2\sigma$  credible intervals of the model fits, respectively. The mock observational datasets used to constrain the models are shown alongside their  $1\sigma$  uncertainties by the various markers and errorbars.

no BHs remaining to the present-day, and the differences in `LIMEPY` models with between  $f_{\text{BH}} = 0$  and  $< 0.1\%$  are nearly indistinguishable (the differences are amplified in Figure 4 by the log-scale).

The initial conditions are also recovered well, however there is a notably larger spread in the inferred quantities. At most, we recover the initial values of mass, radius, density and BH mass fraction to within  $2.5 \times 10^5 M_\odot$ ,  $2$  pc,  $1$  dex and  $1\%$  respectively, with most clusters again performing more accurately than this. In particular, there is a spread among the initial densities, driven largely by smaller discrepancies in the initial radii (which are amplified as  $\rho_h \propto r_h^{-3}$ ), though

<sup>14</sup> Similar figures showing the fits to all models in the sample, as well as full sampler chains, can be found at <http://doi.org/10.11570/26.0014>.

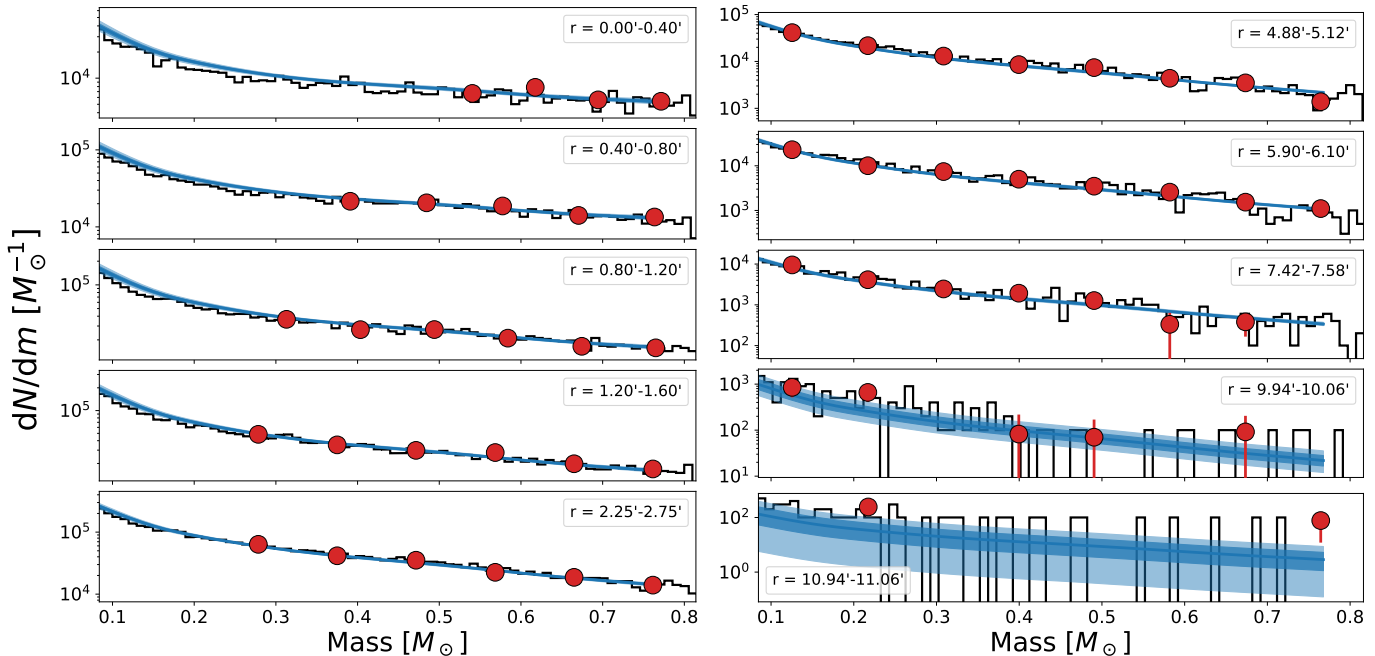


**Figure 2.** Model present-day local stellar mass functions (blue contours) for the fit of the mock observations of the CMC simulation with initial conditions  $N_0 = 8 \times 10^5$ ,  $r_{v,0} = 2$  pc,  $R_G = 2$  kpc and  $Z = 0.0002$ . Each panel shows the number of stars per unit mass as a function of stellar mass, for different projected distance ranges from the cluster centre. The dark and light shaded regions represent the  $1\sigma$  and  $2\sigma$  credible intervals of the model fits, respectively. The mock observational datasets used to constrain the models are shown alongside their  $1\sigma$  uncertainties by the red circles and errorbars. The true underlying mass function from the full CMC snapshot is shown in black.

no strong systematic bias towards higher or lower densities is evident here.

It is likely that most issues in inferring the radii appear due to discrepancies in the `CLUSTERBH` models themselves, when compared to CMC. Due to the fact that our models are constrained only by the present-day observables, any models for which `CLUSTERBH` (when starting with the true initial conditions) under(over)-estimates the final conditions will likely cause our inferred initial conditions to be correspondingly over(under)-estimated, to ensure the correct present-day conditions are recovered. For example, if `CLUSTERBH` slightly underestimates the cluster expansion, recovering the correct present-day radius will require a slight overestimation of the initial radius, to compensate for this discrepancy. In Figure 3, the evolution of `CLUSTERBH` models beginning with the true initial conditions is shown in red, to illustrate this effect. In F26, the `CLUSTERBH` models were typically found to be in agreement with the CMC models to within 20-30 per cent in total mass, half-mass radius and BH mass over their entire evolution, and thus we might expect, at a minimum, corresponding residuals in our recovery of the initial quantities. The agreement between `CLUSTERBH` and CMC also varies across the grid, with some regions of parameter space (e.g.  $r_{v,0} = 4$  pc) expected to exhibit larger residuals than others.

As was found in Section 3.2 of D24, when fitting multimass DF-based models to the same observables, the statistical uncertainties derived from the fitting noticeably underestimate

the overall true uncertainties required in quantities such as the present-day BH mass fraction and the initial mass and radius. As was originally quantified in D24, this underestimation may arise because our procedure operates under the assumption that our models are able to perfectly represent the data, and thus may underestimate the true errors if there is any misspecification between the models we assume and the true underlying models from which the data is generated. Thus we expect that there remain unquantified systematic errors beyond the statistical uncertainties reported here.

Despite these caveats, this validation against mock observations demonstrates that the coupled `cBH+limepy` models provide us with a useful tool, which can reliably predict the initial conditions of GCs based solely on their present-day, observable properties, across a large volume of parameter space.

#### 4. FITTING TO MILKY WAY CLUSTERS

In this section we present the results of applying our fitting procedure, as described in Section 2.4.2, to our full sample of Milky Way GCs, as described in Section 2.4.1.

In Figure 5 and Figure 6, we show an example fit of our models to the observational datasets of the cluster NGC 1851, while in Figure 7 we show the inferred evolution of the mass, radius, density and  $f_{\text{BH}}$  from initial conditions to their present-day values. The best-fitting models provide good fits to the

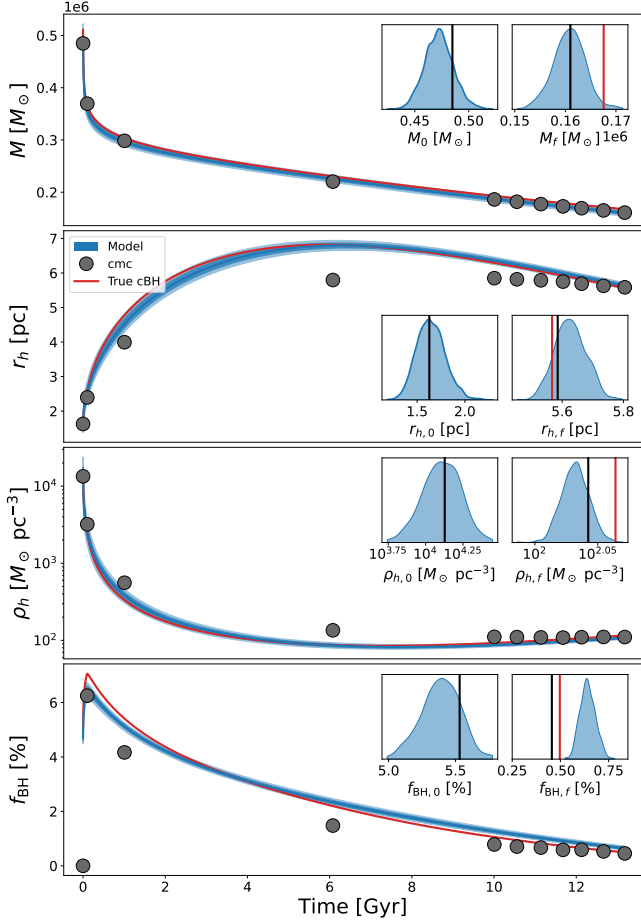


**Figure 3.** Evolution of the model total mass, half-mass radius, half-mass density and BH mass fraction over time (blue contours) for the fit of the mock observations of the CMC simulation with initial conditions  $N_0 = 8 \times 10^5$ ,  $r_{v,0} = 2$  pc,  $R_G = 2$  kpc and  $Z = 0.0002$ . The dark and light shaded regions represent the  $1\sigma$  and  $2\sigma$  credible intervals of the model fits, respectively. The true values from the CMC snapshots are shown as black circles. Note that the models are not fit on these quantities, but they serve to illustrate the recovery of the evolutionary history of the cluster by fitting to the present-day (mock) observations alone. Shown in red is the evolution of a single CLUSTERBH model when initialized with the true initial conditions of the corresponding CMC model. The inset panels show the posterior distributions from our fit of the initial and present-day values of each quantity in blue, with the true values from the CMC models indicated by the black vertical lines.

data in the majority of clusters in our sample<sup>15</sup>. The best-fitting parameter values for all clusters can be found in Table A1, while derived quantities such as the half-mass densities, BH mass fractions, and present-day total mass and half-mass radius can be found in Table A2.

<sup>15</sup> Similar figures showing the fits to all models in the sample, as well as full sampler chains, can be found at <http://doi.org/10.11570/26.0014>.

#### 4.1. Outliers and Unsatisfactory Fits

There are a small number of clusters in our MW sample to which the fits do not reproduce certain observational datasets adequately, or that exhibit other problematic behaviours, which we either flag or remove from our sample entirely. These fits are discussed below.

In certain clusters the stellar mass function data, which consists of various HST pointings divided into radial slices, include multiple fields which overlap with one another in projected distance from the cluster centre. In these cases, the local mass functions are not always entirely consistent with each other within the same radial bin. This may reflect inconsistencies in the stellar photometry or isochrone fitting of H. Baumgardt et al. (2023). In most of these cases, such as in NGC 5904, NGC 6752 or NGC 7099, the differences are small enough that they do not seriously affect the fits, given our mass function nuisance parameter  $F$  accounting for such systematic uncertainties. However, in NGC 6656, these discrepancies are severe enough that the fits to the data are unsatisfactory, and we therefore remove this cluster from our sample.

A few clusters in our sample do not adequately reproduce the kinematic data (and thus the dark mass). This often occurs due to a lack of data in some dimension (e.g. PM or LOS dispersion profiles), which may lead to the overfitting of other datasets such as the mass function or density profiles. We therefore also remove NGC 288, NGC 5927 and NGC 6981 from our sample.

Several clusters in our sample are also classified as “core-collapsed” by, e.g., S. C. Trager et al. (1995). As was described in more detail in D24, visibly core-collapsed clusters are expected to harbour few, if any, BHs today as, in the presence of a BH subsystem, the efficient heat transfer from BHs to stars causes the visible core to remain large relative to  $r_h$ , preventing the collapse of the visible stars until nearly all BHs have been ejected (M. Giersz & D. C. Heggie 2009; P. G. Breen & D. C. Heggie 2013; S. Chatterjee et al. 2013; K. Kremer et al. 2020a). However, as shown in Section 4.3, for some of our core-collapsed clusters (e.g. NGC 7078) we do infer a significant number of BHs. Core-collapsed clusters have cuspy inner surface brightness profiles, which may be difficult to reproduce with LIMEPY models, as they are cored by definition. These clusters also stand out as the only ones which stray notably from the theoretical  $r_c - f_{\text{BH}}$  relationship. In D24 we conducted a separate analysis with these clusters by fixing their BH retention to 0; however, this would be difficult to recreate under the present methodology, as the BH retention is tied to the evolution of the other model parameters, rather than set independently. Therefore, the fits to these clusters, especially those inferring significant BH populations, should be regarded with caution. All core-collapsed clusters are denoted by an asterisk in the rest of this manuscript.

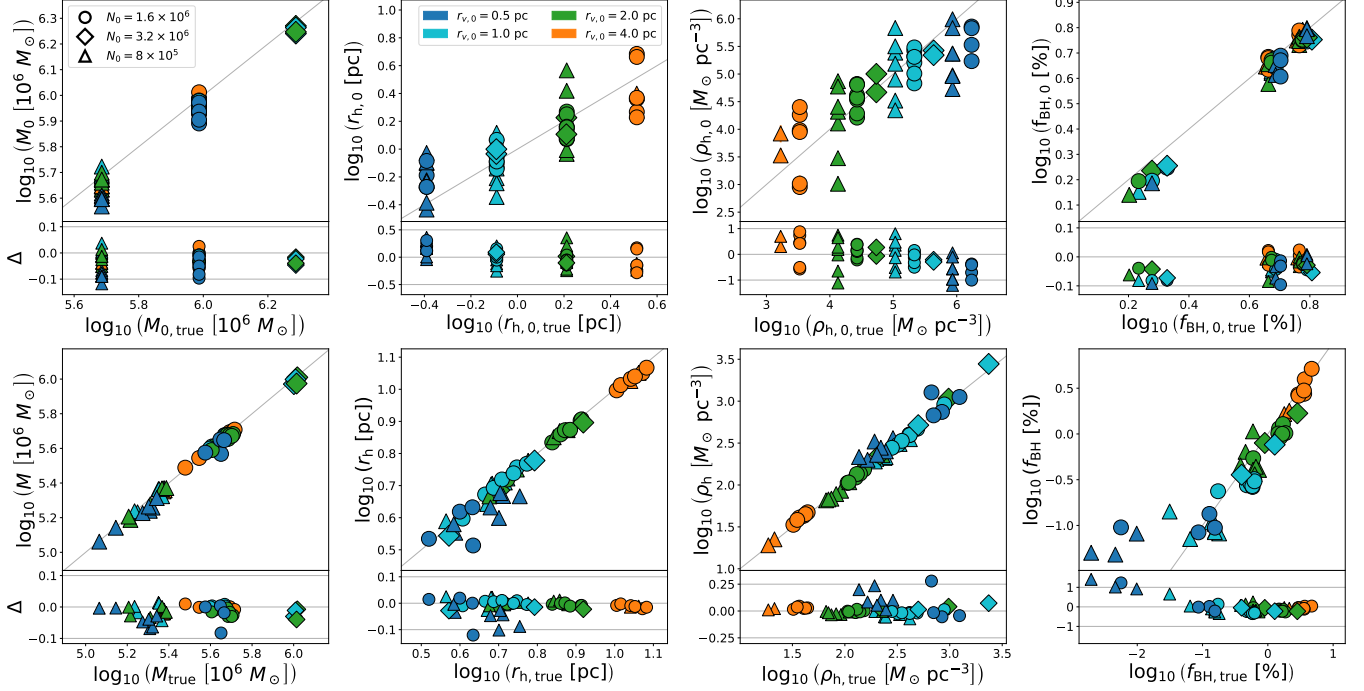


**Figure 4.** Comparison of the initial (top row) and present-day (bottom row) values of the total mass, half-mass radius, half-mass density and mass fraction in BHs inferred by our best-fitting models (on the y-axis), against the true values from the CMC models (on the x-axis). The points are coloured based on their true initial radii, and shown by a diamond, circle or triangle based on their initial number of stars ( $N_0 = [32, 16, 8] \times 10^5$ , respectively). Note that, due to the coarse snapshot time resolution available in the public CMC grid, the  $f_{\text{BH},0}$  values are not taken directly from the CMC snapshots but are instead recomputed based on the true initial CMC conditions using the same SSPROOLS methods as in our models. This allows for the most direct comparison between the inferred and true values. The residuals (inferred minus true, in dex) are shown as a function of the true values below each panel.

Finally, there is one model assumption which is not captured in the fits to mock data which could notably affect our fits to the real clusters: the cluster orbits. While we place our GCs on circularized orbits within a simple isothermal sphere potential, in reality over their entire lifetimes the orbits of clusters may see them interact with galactic substructures, sink towards the galactic centre via dynamical friction, be accreted from ex-situ sources, or pass through the galactic disc. Likewise, the orbital parameters we take from E. Vasiliev & H. Baumgardt (2021) have associated uncertainties, which would only increase when extrapolated further back in time, especially as the potential of the galaxy evolves itself. For most clusters (excluding significant perturbations by structures about which we have no knowledge), where the tides do not dominate the mass loss, small changes in the effective galactocentric radius do not have strong impacts on the evolution or the parameters we infer. However, the impacts of slight changes in  $R'_G$  increase as  $R'_G$  decreases. Some clusters with notably small effective galactocentric radii ( $R'_G \lesssim 1.5$  kpc; well below the range covered by the CMC grid used to validate our models) are thus particularly sensitive to uncertainties in their orbital parameters and history. For example, testing demonstrates that an increase of the  $R'_G$  of NGC 6121 of only 0.2 kpc (up to  $R'_G \sim 1.3$  kpc) can result in an increase

in the inferred initial density of around 0.5 dex. This is further supported by comparison with Monte Carlo modelling of this cluster from D. C. Heggie & M. Giersz (2008), where it was placed at a higher orbit, and yielded a significantly more compact initial size ( $r_{h,0} = 0.58$  pc, compared to our  $r_{h,0} = 1.7$  pc). At these small galactocentric distances, the discrepancies between our chosen model of the galactic potential (which has no defined core) and the true MW potential, may also become more apparent. Given this, the fits to these clusters should therefore be regarded with increased caution. All clusters with notably small  $R'_G$  are denoted by a dagger in the rest of this paper. This especially includes NGC 6093, NGC 6121 and NGC 6266, which are all prominent outliers in our inferred initial density distribution (see Section 4.5). NGC 6624, the cluster in our sample with the smallest  $R'_G$  (0.5 kpc), was unable to be fit by the models at all, and is removed from our sample entirely.

This leaves us with a final cluster sample of 35 MW GCs, which are used in all subsequent analysis.

#### 4.2. Comparison with Validation Sample

In Figure 8, we show Gaussian kernel density estimates of the overall distributions of the inferred initial and present-day mass, radius, density and BH mass fraction, across the fits

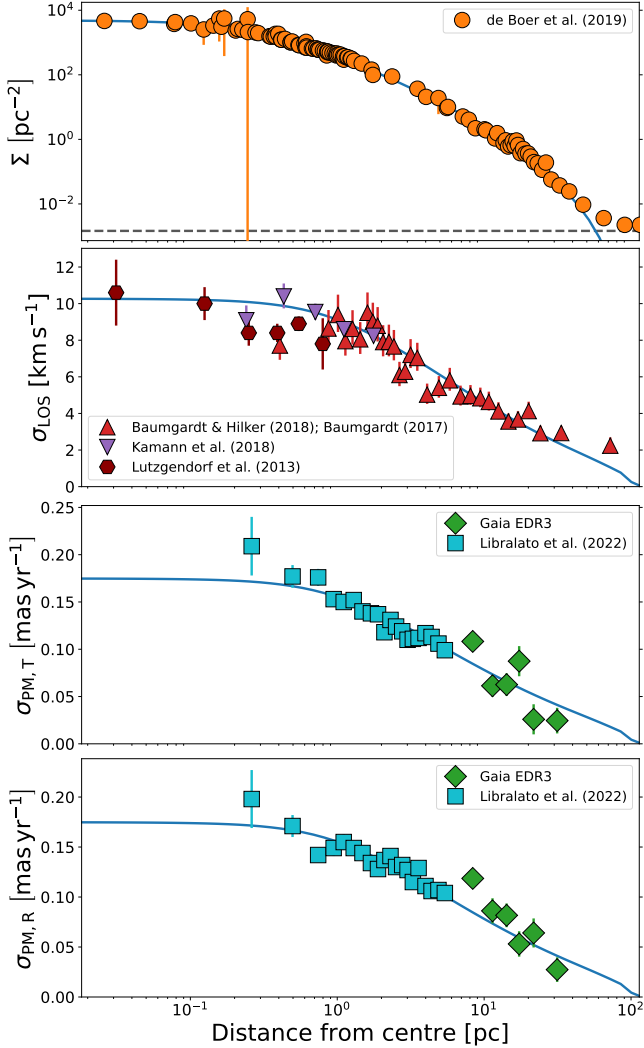


**Figure 5.** Model radial profiles (blue contours) of surface number density ( $\Sigma$ ), line-of-sight velocity dispersions ( $\sigma_{\text{LOS}}$ ), radial ( $\sigma_{\text{PM,R}}$ ) and tangential ( $\sigma_{\text{PM,T}}$ ) proper motion dispersions, for the fit of NGC 1851. The dark and light shaded regions represent the  $1\sigma$  and  $2\sigma$  credible intervals of the model fits, respectively. The observational datasets used to constrain the models are shown alongside their  $1\sigma$  uncertainties by the various markers and errorbars. The background level subtracted from the number density profile is shown by the dashed line.

to all clusters in our sample. Above each panel, we show the values of the corresponding quantities from the CMC validation sample (Section 3), as well as the distributions of our fits to these mock CMC clusters, allowing comparison with both the CMC grid and the expected fitting performance characterised in Section 3.

In particular, it is interesting to note that our inferred present-day cluster masses and radii (and thus densities) for the real clusters generally fall within the range encompassed by the CMC model sample. The CMC grid has been shown to roughly cover the volume of observed present-day cluster

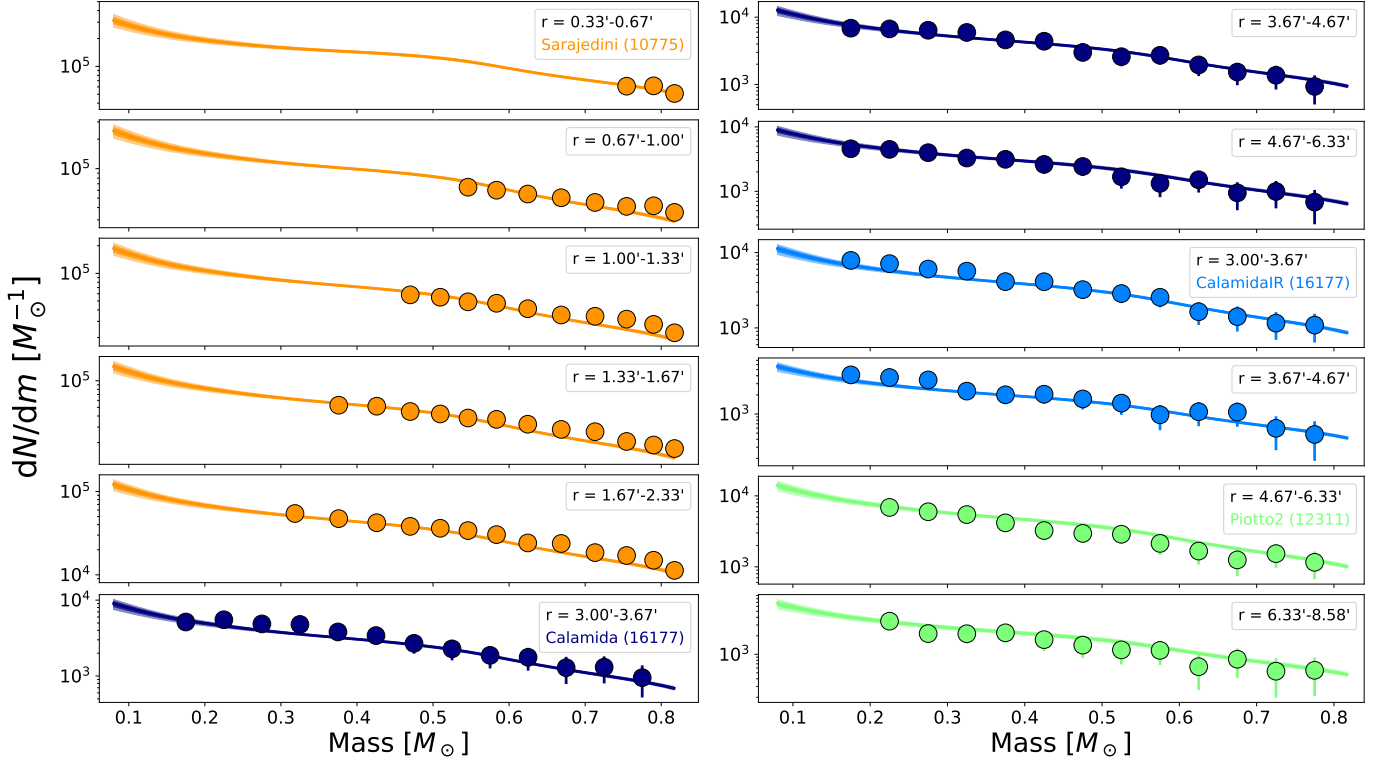
conditions (K. Kremer et al. 2020b), and indeed our inferred results for individual clusters agree closely with other literature studies, for example with the total masses and half-mass radii from H. Baumgardt et al. (2023).

When we compare the initial conditions, however, certain quantities shown in Figure 8, most notably the densities and BH mass fractions, diverge from the CMC models. The initial BH mass fractions fall towards the higher end of the CMC grid, and frequently exceed even the maximum values seen in the grid, by around 1 to 2 per cent. As we use the same BH kick prescriptions and IFMRs here, this difference is attributable both to the fact that our MW sample consists of relatively metal-poor GCs (there are no clusters in our sample nearly as metal-rich as the  $Z = 0.02$  CMC models), and to our inferred IMF (discussed in more detail in Section 4.4), both of which lead to an increased initial BH mass fraction. On the other hand, the majority of the inferred present-day BH mass fractions are small, typically less than 1.5 per cent (discussed in more detail in Section 4.3).

Most interestingly, the initial radii are typically inferred to be quite small ( $\lesssim 0.7$  pc), and in turn the initial cluster densities can often be notably higher than those found in even the densest of CMC models. This is discussed in more detail in Section 4.5. Importantly though, as was mentioned in Section 3, while there is a spread in how well we recover the initial radii (and thus density, of about 1 dex) in our mock validation fits, at the lowest radii tested ( $r_{v,0} = 0.5$  pc), we tend to slightly *overestimate* the initial radii (and thus underestimate the density). Therefore, it is unlikely that these very small initial radii and high densities are the result of a corresponding bias in our fitting, but instead are genuinely required to fit the the available data. It must also be noted, however, that as the CLUSTERBH models are calibrated against the CMC grid, the behaviour of our models beyond the density regimes covered by the grid cannot be tested directly, and we must trust that the physical prescriptions used extrapolate correctly to higher densities. Nonetheless, even if we are less confident in the models in this regime, it is also true that if the observations were consistent with initial conditions more closely resembling those of the CMC grid, we *would* expect to recover those, as demonstrated in Section 3. Therefore, the fact that the data does not prefer models in this regime is itself indicative of higher required initial densities.

#### 4.3. Black Hole Populations

In this section we explore the populations of BHs present in our sample of clusters today, as inferred from our best-fitting models, and compare our results with previous studies. The observational data we use provides direct constraints on both the phase-space distribution of visible stars and the total cluster mass, and thus provides an indirect way of constraining the dark mass, including BHs, present today.



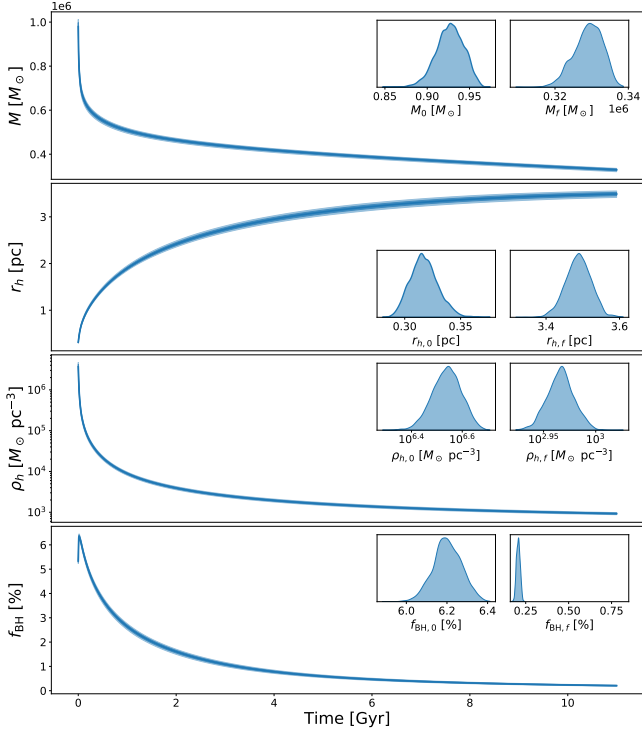
**Figure 6.** Model present-day local stellar mass functions for the fit of NGC 1851. Each panel shows the number of stars per unit mass as a function of stellar mass, for different projected distance ranges from the cluster centre. The dark and light shaded regions represent the  $1\sigma$  and  $2\sigma$  credible intervals of the model fits, respectively. The measurements used to constrain the models are shown alongside their  $1\sigma$  uncertainties by the circles and errorbars. The panels are colour-coded by the *HST* program used, with the PI name and identifier listed in the top-right corners. Note that some programs overlap in their radial coverage.

Figure 9 shows the inferred posterior probability distributions of the mass fraction ( $f_{\text{BH}}$ ) and total mass ( $M_{\text{BH}}$ ) in BHs retained to the present-day in our best-fitting models of all clusters in our sample. Most clusters are consistent with retaining relatively few BHs to their current ages, with BH mass fractions below 1 per cent in the majority of clusters. A minority of clusters have slightly higher inferred BH mass fractions, between 1 and 2 per cent. Finally, a small number of clusters have notably larger BH populations, greater than 2 per cent and extending up to nearly 4 per cent at the maximum (excluding  $\omega$  Cen), though it should be noted that NGC 6121 ( $f_{\text{BH}} \sim 3.5\%$ ) is one of the clusters with  $R'_G < 1.5$  kpc and should be interpreted with caution.

Also shown in Figure 9 is the comparison between our inferred BH masses and mass fractions and those from D24, N. C. Weatherford et al. (2020) and A. Askar et al. (2018). While, generally speaking, we reach broadly similar conclusions as in D24, namely that most clusters harbour relatively small populations of BHs today, our inferred BH mass fractions are consistently higher than in D24. We find a number of clusters with  $f_{\text{BH}} \gtrsim 1$  per cent, with the bulk of our results ( $\sim 85$  per cent) lying below  $f_{\text{BH}} = 1.5$  per cent, whereas D24 instead found only one cluster with  $f_{\text{BH}}$  above 1 per cent ( $\omega$  Cen), with most below  $f_{\text{BH}} = 0.4$  per cent. On an

individual level, very few of the clusters are mutually consistent between D24 and here, within their uncertainties, except where both infer very small  $f_{\text{BH}}$ . We note again, however, that only the statistical uncertainties are reported in both studies, and the true uncertainties are likely larger. Based on the results of Section 3, the present-day  $f_{\text{BH}}$  values may be expected to be accurate to within 1 per cent at  $f_{\text{BH}} \sim 2.5$  per cent, at worst. While this is a rough estimate, it illustrates how underestimated the reported uncertainties likely are.

N. C. Weatherford et al. (2020) predicted the amount of BHs in these clusters today by comparing the level of visible mass segregation against the anticorrelation with  $f_{\text{BH}}$  seen in CMC models by N. C. Weatherford et al. (2018), while A. Askar et al. (2018) used correlations found by M. Arca Sedda et al. (2018) between the density of inner BH-subsystems and the central surface brightness of the clusters in the MOCCA survey database. Given to the larger uncertainties in these studies, many of our clusters agree, within  $2\sigma$ , with the present-day masses in BHs inferred by these studies, though a number of discrepancies remain between specific clusters, and in particular, as with the comparison to D24, there are a number of clusters for which we now infer higher mass fractions in BHs.



**Figure 7.** Evolution of cluster total mass, half-mass radius, half-mass density and BH mass fraction over time for the fit of NGC 1851. The dark and light shaded regions represent the  $1\sigma$  and  $2\sigma$  credible intervals of the model fits, respectively. The inset panels show the posterior distributions from our fit of the initial and present-day values of each quantity.

It is worth highlighting the differences in approach between D24 and this work in recovering the present-day BH populations. While the inference of the remnant populations in both are dictated by the total and visible mass constraints set by the observational data, and the same family of equilibrium models are used to fit the present-day structure, in D24 the final amount of BHs retained was almost entirely set by a freely varying BH retention fraction parameter ( $\text{BHret}$ ), which controlled the total amount of dynamically ejected BHs, independent of all other parameters. In this work, however, there is no such BH retention parameter; instead, the initial mass fraction in BHs is set by the IMF, the BH IFMR and the BH natal kicks, while the subsequent rate of dynamical ejections over the cluster lifetime is modelled by `CLUSTERBH`, where it is coupled to the energy demands of the cluster as a whole. Thus, the final amounts of retained BHs we infer here are self-consistently constrained not only by the observational data, but by the required evolution of the rest of the cluster properties as well.

Overall, these extra physically-motivated constraints should provide more confident inferences of the possible present-day BH populations. However, this reduction in freedom comes at the cost of additional modelling assumptions, some of which

are governed by uncertain physical prescriptions. We have demonstrated that our models typically recover the BH populations of CMC simulations well (Section 3); however, since the CMC models share the same underlying BH assumptions (e.g. IFMR and natal kick prescriptions), this validation cannot be used to say whether those assumptions are valid for real clusters. One further avenue for addressing this would be to explore a wider range of the assumptions underlying BH formation, while still self-consistently modelling the evolution of the BH population. This is discussed in Section 5.6 and will be explored in more detail in a forthcoming paper. The fits to the observational data are similarly good in both this work and D24, even though the best-fitting models may diverge from one another slightly in the central velocity dispersions (particularly when we infer larger BHs amounts), where signatures of BH populations should appear. However, the leverage provided by the BH signatures in the central kinematics is highly dependent on the quality and quantity of the central kinematic data available, and in most clusters the current data is insufficient to confidently distinguish the presence of BHs to a precision of  $f_{\text{BH}} \lesssim 0.5$  per cent at  $f_{\text{BH}} \sim 1$  per cent, as would be required to truly discriminate between our results and those of D24 in most clusters, given we know that the overall uncertainties in both are underestimated.

One cluster which may possess good enough kinematic data to better constrain its BH population is  $\omega$  Cen (e.g. A. Zocchi et al. 2019), especially with the addition of new, deep kinematic data from M. Häberle et al. (2025). However, the presence of several fast-moving stars in this new dataset has also been used to argue for the presence of a  $\gtrsim 10^4 M_{\odot}$  IMBH in the cluster core (M. Häberle et al. 2024). As discussed in D24, we cannot currently directly include the potential of an IMBH in our `LIMEPY` models to test this, and it is unclear how the presence of an IMBH would affect our evolutionary modelling, but our inferred mass in BHs ( $M_{\text{BH}} = 2.51^{+0.003}_{-0.002} \times 10^5 M_{\odot}$ ) is significantly higher than the IMBH mass range reported by M. Häberle et al. (2024), which still suggests the presence of a significant population of stellar-mass BHs in the cluster. We also note that, given the possible origin of  $\omega$  Cen as the accreted nuclear star cluster of a disrupted dwarf galaxy (e.g. K. Bekki & K. C. Freeman 2003; A. Meza et al. 2005), the tidal history of this cluster may be more complex than can be accounted for in our models.

#### 4.4. Initial Mass Function

In this section we explore the shape of the stellar IMF inferred from our fits. We place direct constraints on the IMF below  $1 M_{\odot}$  by allowing the power-law slopes of  $\alpha_1$  and  $\alpha_2$  to vary freely.

In Figure 10 we show the inferred values of the IMF slopes below  $1 M_{\odot}$ . This figure clearly shows that our inferred IMF does not match that of P. Kroupa (2001), a commonly adopted

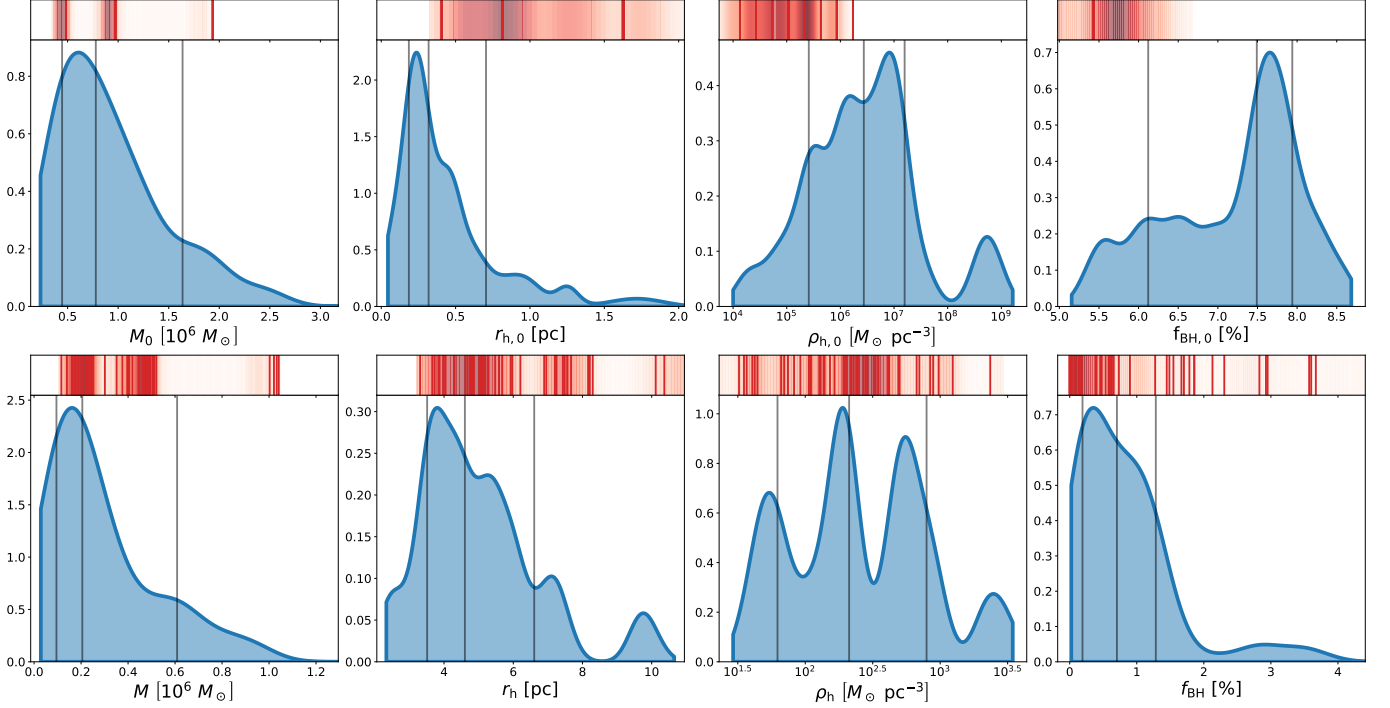


**Figure 8.** Gaussian kernel density estimates showing the overall distributions of the initial (top row) and final (bottom row) total mass, half-mass radius, half-mass density and BH mass fractions across the fits to all clusters in our sample. Median and  $1\sigma$  intervals are shown by the black lines. Above each panel the corresponding values for all of the CMC models included in our validation sample (Section 3) are shown as red vertical lines, while the density distributions of these quantities from our fits to the mock CMC models are shown as the red shaded regions. The mass and present-day  $f_{\text{BH}}$  axes are truncated such that  $\omega$  Cen is not visible to the far right ( $M_0 = 6.81 \pm 0.04 \times 10^6 M_\odot$ ,  $M = 5.62 \pm 0.02 \times 10^6 M_\odot$ ,  $f_{\text{BH}} = 8.31 \pm 0.06 \%$ ), and not all CMC values are visible, in order to better highlight the distributions of the rest of the sample.

IMF prescription which is used in most cluster modelling, including the CMC grid itself. Our inferred IMF is notably more bottom-light, i.e. deficient in low-mass stars, relative to the P. Kroupa (2001) IMF. This is in line with the findings of H. Baumgardt et al. (2023), though as also shown in Figure 10 our inferred slopes differ from theirs as well. Over our full MW cluster sample we find median and  $1\sigma$  values of  $\alpha_1 = 0.82^{+0.27}_{-0.20}$  and  $\alpha_2 = 1.47^{+0.45}_{-0.41}$ , in comparison with the values of  $\alpha_1 = 0.3$  and  $\alpha_2 = 1.65$  for H. Baumgardt et al. (2023) and  $\alpha_1 = 1.3$  and  $\alpha_2 = 2.3$  for P. Kroupa (2001). We note, however, that H. Baumgardt et al. (2023) use a slightly different break mass in this regime of  $0.4 M_\odot$  compared to our  $0.5 M_\odot$ , and an IMF upper mass limit of  $100 M_\odot$  compared to our limit of  $150 M_\odot$ . These slopes are also similar to those found for the least dynamically evolved clusters in D23 (see their Figure 8). The slopes inferred there effectively represent the present-day mass function rather than the true IMF, as no prescriptions were employed to account for the tidal losses of stars, which preferentially affects the low-mass stars and changes the shape of the mass function over time; however, in the least dynamically evolved clusters, the present-day MF should resemble the IMF most closely.

In Appendix B we demonstrate how these inferred IMF slopes are mainly constrained by the observed stellar mass function data.

This bottom-light IMF has several important implications, in comparison to canonically assumed IMF prescriptions such as P. Kroupa (2001). This IMF yields a notably higher initial mean stellar mass ( $\sim 0.97 M_\odot$ , compared to  $0.58 M_\odot$  under P. Kroupa 2001). It also results in a nearly 25 per cent increase in the number of BHs formed, per unit cluster mass. This is largely the reason why, as noted in Section 4, our best-fit models typically have higher initial BH mass fractions (peaking near  $f_{\text{BH},0} \simeq 7.7\%$ ) than in, e.g., the CMC grid.

#### 4.5. Initial Conditions

One of the most important results enabled by our new models is the inference of the clusters' initial conditions: total mass, half-mass radius and density. As described in Section 2 and tested in Section 3, we directly infer these quantities as free parameters in our fitting, constrained by the observational constraints on their present-day counterparts, and the evolutionary history implied by CLUSTERBH.

The distributions of the inferred initial conditions across our fits are shown in the top row of Figure 8, while Figure 11 shows the median initial cluster mass and half-mass radius

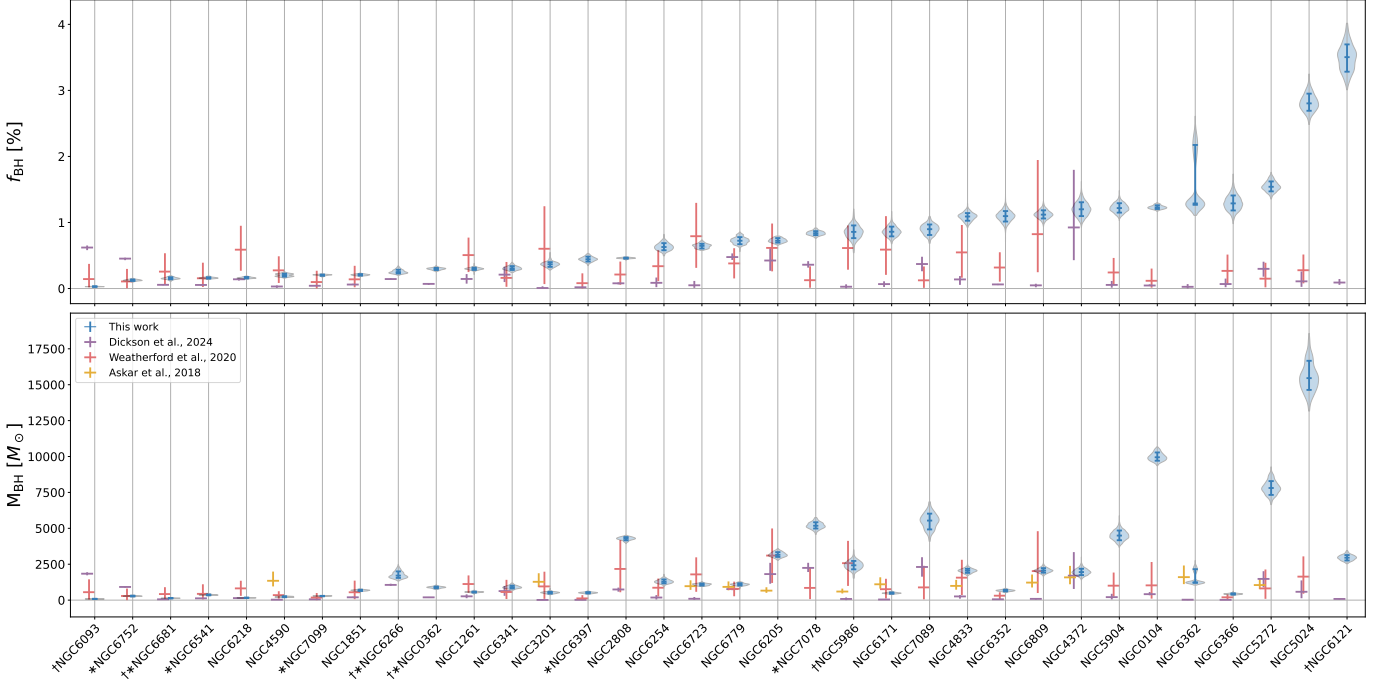


**Figure 9.** Violin plots (in blue) of the posterior probability distribution of the mass fraction in BHs ( $f_{\text{BH}}$ ; upper panel) and the total mass in BHs (lower panel) for all clusters in our sample, except for NGC 5139 ( $\omega$  Cen), which has  $f_{\text{BH}} \sim 8.3$  per cent, and is excluded in order to better highlight the distributions of the other clusters. The median and  $1\sigma$  intervals are denoted by the horizontal blue ticks within each distribution. These errors represent only the statistical uncertainties on our fits, and thus are likely underestimated. Clusters are sorted by  $f_{\text{BH}}$ . All clusters classified as core-collapsed in *S. C. Trager et al. (1995)* are denoted by an asterisk. All clusters with  $R'_G < 1.5$  kpc are denoted by a dagger. The median and  $1\sigma$  intervals from D24 (purple), *N. C. Weatherford et al. (2020)* (red), and *A. Askar et al. (2018)* (orange), are also shown for all clusters in common with our sample. Values from *N. C. Weatherford et al. (2020)* are computed using the median clustercentric mass segregation parameter  $\Delta_{r,50}$  (Table 1 of *N. C. Weatherford et al. (2020)*), and conversions between total masses in BHs and mass fractions are computed using our total cluster mass estimates.

for each cluster, as well as their evolutionary tracks over the age of the cluster to their present-day values. The individual quantities for each cluster are also listed in Tables A1 and A2.

The majority of our clusters have initial total masses within a range of  $0.4 - 2 \times 10^6 M_\odot$ , while the initial radii are typically less than 0.7 pc, with the overall distribution peaking around 0.25 pc. In many clusters, these compact initial sizes result in very high initial densities. The overall distribution of  $\rho_{h,0}$  has a median value of about  $10^{6.4} M_\odot \text{pc}^{-3}$  with a  $1\sigma$  width of slightly less than 1 dex. A notable peak can also be seen at much higher densities ( $\sim 10^9 M_\odot \text{pc}^{-3}$ ) in Figure 8, however this is made up of clusters with  $R'_G < 1.5$  kpc (NGC 6093 and NGC 6266), which should be regarded with caution, as discussed in Section 4.1.

Also overlaid in Figure 11 are the initial values of the CMC models used in Section 3. A significant fraction of our clusters have inferred initial densities exceeding even the densest CMC models. As discussed in *K. Kremer et al. (2020b)*, this may partly be simply due to the limits of their simulation grid, due to the high computational costs and stellar collision rates of the densest model.

It is important to note that the distributions shown here of, e.g., initial density reflect only the inferred conditions of the

individual clusters within our sample. The initial conditions of the individual clusters are not drawn from shared parent distributions (e.g. a common cluster mass function) but from independent, uninformative priors, and do not account for, e.g. the populations of initially formed clusters which have dissolved by the present day. Our sample of clusters is also likely biased towards more nearby, massive and denser GCs, and thus not necessarily representative of the entire surviving MW GC population. Therefore, these distributions should not be taken as overall cluster population distributions, but only to demonstrate where the initial conditions of a large sample of the most well-studied MW clusters may lie. The fast models presented here are, however, well suited to this problem, and in a future work we will explore the cluster population distributions directly using hierarchical Bayesian modelling approaches.

## 5. DISCUSSION

### 5.1. Comparison with High Redshift Clusters

With the advent of JWST, it is now becoming possible to compare our modelling predictions with observations of high-redshift candidate proto-GCs in strongly lensed galaxies. In Figure 12, we compare the young GC-like systems discovered

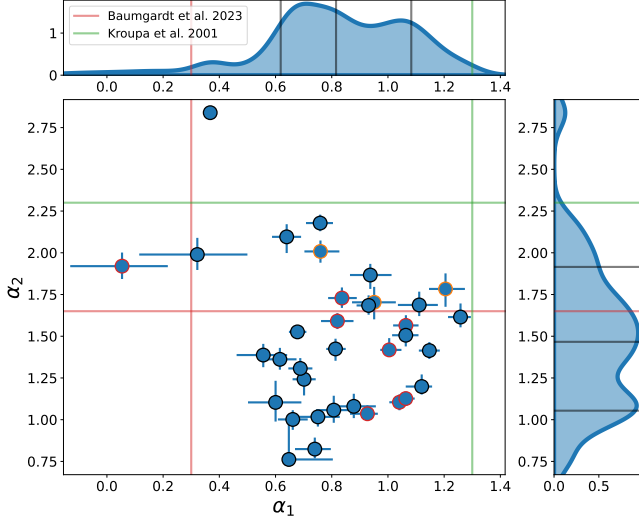


**Figure 10.** The median values and  $1\sigma$  uncertainties of the inferred stellar IMF power-law slopes  $\alpha_1$  and  $\alpha_2$  for all clusters in our sample. Gaussian kernel density estimates showing the overall distributions of each parameter are shown above and to the right. The median values of the corresponding IMF slopes from P. Kroupa (2001) (green) and H. Baumgardt et al. (2023) (red) are shown by the horizontal and vertical lines on each panel. All core-collapsed clusters are outlined in red. All clusters with  $R'_G < 1.5$  kpc are outlined in orange.

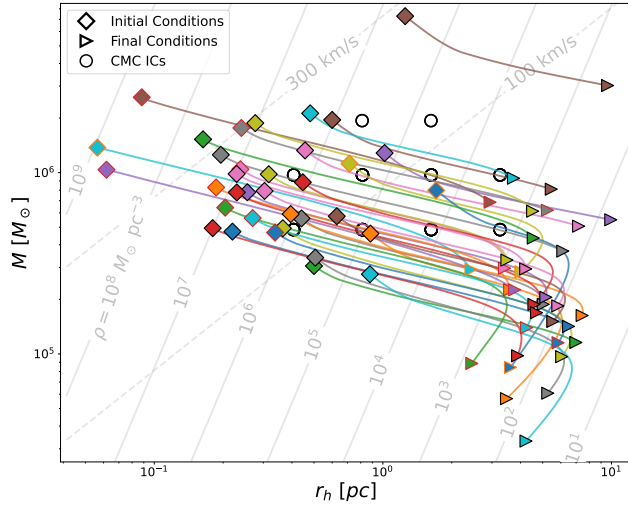


**Figure 11.** Tracks of the evolution of each cluster in our sample, from initial total cluster mass and half-mass radius (square markers) over their lifetimes to the present conditions (triangle markers). Only the median inferred values of each quantity are shown. All colours are assigned randomly, to differentiate the tracks. Lines of constant half-mass density and central escape velocity are shown in grey. The initial values of the sample of CMC models used in Section 3 are also shown as circles. All core-collapsed clusters are outlined in red. All clusters with  $R'_G < 1.5$  kpc are outlined in orange.

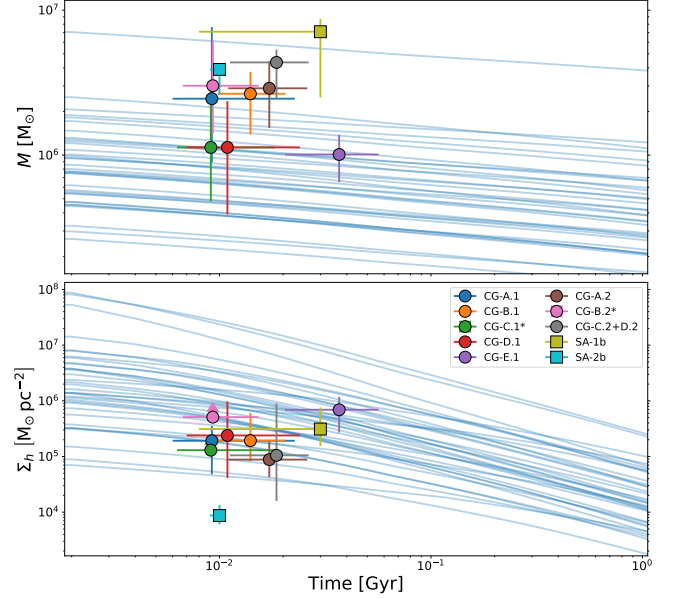


**Figure 12.** Evolution of the inferred total mass (top panel) and average effective surface density (bottom panel) over time for all clusters in our sample (blue lines). Only the median inferred values are shown. The surface density is computed assuming that light follows mass, and by scaling the half-mass radius by 0.75, to approximately account for projection effects. The circle and square markers represent the age, mass and surface density measurements of the “Cosmic Gems” (CG) and “Sunrise Arc” (SA) proto-GCs as presented by A. Adamo et al. (2024) (see their Table 1 and Extended Data Table 2) and E. Vanzella et al. (2023) (see their Table 3, excluding those classified as “nebular knots”), respectively. Clusters denoted with an asterisk represent only lower limits on the density.

by A. Adamo et al. (2024) within the “Cosmic Gems Arc” and E. Vanzella et al. (2023) within the “Sunrise Arc” with the inferred density evolution of our full sample of MW GCs. The bulk of our results are consistent with these observations. All but the densest outliers reach comparable densities to these high-redshift clusters by their estimated ages ( $\sim 20$ – $50$  Myr). This is possible, despite many of our inferred initial densities being higher than those observed, because within the first  $\sim 100$  Myr the density of a cluster can decrease by nearly an order of magnitude as it quickly loses mass and expands. This comparison suggests that our inferred initial densities for MW GCs may be consistent with proto-GCs observed in the early Universe. However, there also remains substantial uncertainties in the physical parameters of these candidate proto-GCs, due to uncertainties in the stellar population and lens modelling (A. Adamo et al. 2024).

## 5.2. Runaway Collisions and IMBH Formation

Here we discuss the consequences of the high initial densities we infer on the formation of an IMBH from a very massive star ( $\gg 100 M_\odot$ ) formed through runaway stellar collisions (e.g., S. F. Portegies Zwart et al. 2004; J. M. Fregeau et al.

2004; K. Sharma & C. L. Rodriguez 2025). Apart from  $\omega$  Cen (M. Häberle et al. 2024), there is currently no compelling evidence for IMBHs in any MW GCs, with current upper limits of  $\lesssim 10^3 M_\odot$  from both dynamics (e.g., H. Baumgardt 2017) and (the absence of) accretion signatures (e.g., E. Tremou et al. 2018).

As a method of estimating the expected IMBH masses which could arise given our densities, we can turn to the results of Monte Carlo and  $N$ -body simulations by M. C. Vergara et al. (2026). These authors demonstrated that above a critical cluster mass ( $M_{\text{crit}}$ ), runaway collisions can lead to IMBHs with masses  $\gtrsim 10^4 M_\odot$ . This  $M_{\text{crit}}$  depends on the initial radius as  $M_{\text{crit}} \propto r_h^{7/3}$ , and if we rewrite this in terms of  $\rho_h$  using their constants of proportionality, we find that the critical *density* for formation of IMBHs with masses  $\gtrsim 10^4 M_\odot$  is

$$\rho_{h,\text{crit}} \gtrsim 10^8 M_\odot \text{pc}^{-3} \left( \frac{M}{10^6 M_\odot} \right)^{-2/7}. \quad (8)$$

All of our inferred initial densities (except for the three highest-density outliers, which as discussed above should all be taken with some caution), fall below this mass-dependent  $\rho_{h,\text{crit}}$ . A. Rantala et al. (2026) similarly explored the formation of IMBHs via runaway collisions within a grid of  $N$ -body models spanning a range of densities. Based on these simulations, the authors presented simple formulae for the expected IMBH masses as a function of cluster surface density and metallicity (see their Equations 9 and 10). Applying these functions to our inferred surface densities results in IMBH masses in the range of around 1000 to 3500  $M_\odot$ . Comparison with these studies thus suggests that, even given our notably higher inferred initial densities, we might not expect to see very massive IMBHs ( $\gtrsim 10^4 M_\odot$ ) form in GCs through this mechanism.

V. Bocchi et al. (2026) presented another method for estimating the potential IMBH masses in dense clusters by employing Fokker-Planck models, and applied this to high-redshift clusters. For the COSMIC Gems and Sunrise proto-GCs (Section 5.1), they estimated IMBH masses of around  $(1 - 3) \times 10^3 M_\odot$ . Given that many of our clusters match the densities of these proto-GCs, this may suggest that similar IMBH masses could form within them as well.

There are, however, a number of caveats related to this analysis. First, stellar collisions may be far more efficient if the IMF were to extend up to much larger masses (e.g.  $\sim 10^3 M_\odot$ ), as was recently proposed by M. Gieles et al. (2025) to explain the multiple stellar population of GCs. On the other hand, collisions between stars and very/extremely massive stars are not well studied, and significant uncertainties remain. For example, these collisions may actually lead to a net stripping of mass (L. Ramírez-Galeano et al. 2025; J. Roman-Garza et al. 2026). Whether these collisions add or remove mass depends

sensitively on the structure of very/extremely massive stars, which is itself also very uncertain. Furthermore, as noted in Section 4.5, our own evolutionary models come with the caveats that we do not account for these collisions or IMBH formation.

In summary, given our high inferred initial densities, we may expect stellar collisions to occur and potentially lead to the formation of IMBHs with masses  $\lesssim 10^3 M_\odot$ . However, it is not possible for us to place strong constraints on this process.

### 5.3. IMBH Formation Through Hierarchical BH Mergers

An alternative pathway to IMBH formation in GCs is through repeated, or “hierarchical”, BH mergers (e.g., F. Antonini & F. A. Rasio 2016; C. L. Rodriguez et al. 2018; M. Mapelli et al. 2021) Here we consider the implications of our inferred initial conditions for IMBH formation via hierarchical BH mergers.

Whether this occurs depends critically on the initial escape velocity of the GC ( $v_{\text{esc},0}$ ), which must be high enough to retain the first few BBH merger products after the gravitational wave (GW) recoil kicks they receive during each merger. These kicks are particularly large for near equal-mass mergers (hundreds of  $\text{km s}^{-1}$ ). Subsequent mergers have smaller mass ratios and receive smaller GW kicks, allowing the most massive BH to continue to grow. F. Antonini et al. (2019) showed that an IMBH could grow in this way in GCs with  $v_{\text{esc},0} \gtrsim 300 \text{ km s}^{-1}$ . The final IMBH mass then scales nearly linearly with GC mass as  $M_{\text{IMBH}} \approx 2 \times 10^{-3} M$ , with a weak dependence on initial density (see their equation 21). Similar conclusions were reached by S. Torniamenti et al. (2026).

Figure 11 shows that three of our clusters (NGC 6093, NGC 6266 and NGC 6752) have  $v_{\text{esc},0} \gg 300 \text{ km s}^{-1}$ , however, as noted in Section 4.1, each of these three should be treated with caution. Five other clusters (NGC 5139, NGC 5904, NGC 6205, NGC 7078\*, NGC 7089\*) have initial escape velocities approaching this limit ( $v_{\text{esc},0} > 250 \text{ km s}^{-1}$ ). Of these, only NGC 5139 ( $\omega$  Cen) has compelling evidence for an IMBH, and the expected IMBH mass in the hierarchical merger scenario ( $\sim 1.6 \times 10^4 M_\odot$ ) is consistent with the inferred IMBH mass of M. Häberle et al. (2024). For the other GCs, no conclusive evidence of IMBHs has been presented, though expected IMBH masses of a few times  $10^3 M_\odot$  in lower-mass GCs cannot always be ruled out (e.g., B. J. McNamara et al. 2012; M. den Brok et al. 2014).

In summary, our inferred initial conditions suggest that hierarchical BH mergers could present a viable avenue for IMBH growth in a small number of MW GCs, however for the majority of clusters (where  $v_{\text{esc},0} < 300 \text{ km s}^{-1}$ ), this channel is unlikely.

#### 5.4. Maximum Allowed Surface Densities

It has been suggested, based on the maximum density observed in dense stellar systems today across many orders of magnitude (P. F. Hopkins et al. 2010) and on theoretically expected equilibrium states between feedback and gravity (R. M. Crocker et al. 2018; M. Y. Grudić et al. 2019), that there is an upper limit expected on the initial stellar surface densities of newly formed star clusters. While the proposed maximum values vary slightly, a rough upper limit slightly above of  $\sim 10^5 M_{\odot} \text{pc}^{-2}$  has been proposed. For nearly every cluster in our sample, our inferred initial surface densities clearly exceed these proposed limits. While our modelling does have the caveat that we simplify the very beginnings of our cluster evolution by assuming all of the surrounding gas has been cleared (at time 0), it is nonetheless true that much higher initial stellar densities are clearly able to recreate the GCs we observe today, and are in fact preferred by the data. Similarly, as discussed in Section 5.1, more recent observations of high-redshift proto-GCs may also lie above this limit, even after  $\sim 50$  Myr of evolution (A. Adamo et al. 2024; E. Vanzella et al. 2023).

#### 5.5. Implications for Gravitational Wave Sources

The density of star clusters is an important parameter in setting the rate of dynamically-formed BBH mergers, with denser clusters generating more BBH mergers (e.g., C. L. Rodriguez et al. 2016). Here we consider whether our inferred initial densities are consistent with the BBH merger rate determined by LIGO-Virgo-KAGRA (LVK). The population models of F. Antonini & M. Gieles (2020b) show that the dynamical BBH merger rate at low redshift increases with initial GC density up to densities of  $\sim 10^5 M_{\odot} \text{pc}^{-3}$ , beyond which the merger rate plateaus and even decreases slightly for densities  $\gtrsim 10^7 M_{\odot} \text{pc}^{-3}$  as BBH mergers in denser GCs tend to occur at higher redshifts. The maximum dynamical merger rate in their models is well below the total merger rate inferred by LVK, and therefore our inferred densities do not imply an overproduction of dynamical BBH mergers.

Denser clusters also give rise to a steeper redshift dependence for the merger rate (see Figure 4 of F. Antonini & M. Gieles 2020b), with densities of  $\sim 10^6 - 10^7 M_{\odot} \text{pc}^{-3}$  (in line with our results) leading to a redshift dependence consistent with recent LVK findings (GWTC-5.0; The LIGO Scientific Collaboration et al. 2026).

Finally, initial densities of  $\gtrsim 10^5 M_{\odot} \text{pc}^{-3}$  are needed to explain the most massive BHs in the pair-instability gap with hierarchical mergers in GCs (F. Antonini et al. 2023).

In summary, population models of GCs seem to favour initial densities similar to those we infer here, in order to explain some features of the observed GW data.

#### 5.6. Implications for BH Physics

The high initial densities we infer could also instead reflect underlying issues in some of the prescriptions used within our models, and which are also commonly assumed in many other dynamical models. The constraints on the present-day conditions from the observations, notably the central kinematics and stellar mass functions, require both an IMF that is deficient in low-mass stars, and thus enriched in BHs progenitors (as discussed in Section 4.4; see also D23 and H. Baumgardt et al. 2023), and in most clusters relatively small populations of BHs retained to the present day (as discussed in Section 4.3). In order to achieve this, while also reproducing the total masses and radii observed today, a very high rate of BH ejections from the cluster is required. Within our current framework, the only viable method for accomplishing this is to increase the rate of early dynamical ejections by substantially increasing the initial densities and shortening the relaxation times.

However, this is not the only way by which the large required depletion of the initial BH population could be achieved. The BH natal kicks also provide a mechanism for ejecting the BHs immediately after their formation. Stronger kicks could allow a cluster to deplete the populations of BHs and yield the required present-day conditions, without requiring a higher initial density. Similarly, a different BH IFMR could reduce the initial mass in BHs formed from our bottom-light IMF, alleviating this issue. The BH natal kick and IFMR prescriptions that we use here (as described in Section 2) are both commonly used by many other cluster modelling works, but they remain uncertain (L. Boccioli & G. Fragione 2024; S. Popov et al. 2025).

To demonstrate this, we conduct a simple experiment using `CLUSTERBH`. We start with a fiducial set of initial conditions ( $M_0 = 10^6 M_{\odot}$ ,  $\rho_{h,0} = 10^6 M_{\odot} \text{pc}^{-3}$ ,  $[\text{Fe}/\text{H}] = -2$ ,  $R'_G = 5 \text{ kpc}$  and the median inferred IMF slopes from Section 4.4) and, instead of the canonical kick prescription used in this paper, we reduce the initial BH mass by a fraction  $f_k = 50\%$ , and then evolve this model for 12 Gyr. We then consider a grid of initial densities, spanning an order magnitude in either direction ( $\rho_{h,0} \in [10^5, 10^7] M_{\odot} \text{pc}^{-3}$ ), hold all other parameters fixed, and determine for each density the value of  $f_k$  that leads to an evolution which minimizes the distance between the present-day values of the total mass, radius, and BH mass fraction of the fiducial and modified models. This yields a relationship between the initial density and the strength of the natal kicks which produces a nearly identical cluster at the present day.

The results of this experiment are shown in Figure 13, where we can see that a change in kick strength of approximately 40 per cent, in either direction, can compensate for an order-of-magnitude change in initial density in the opposite direction, and result in very similar models at the present day. This

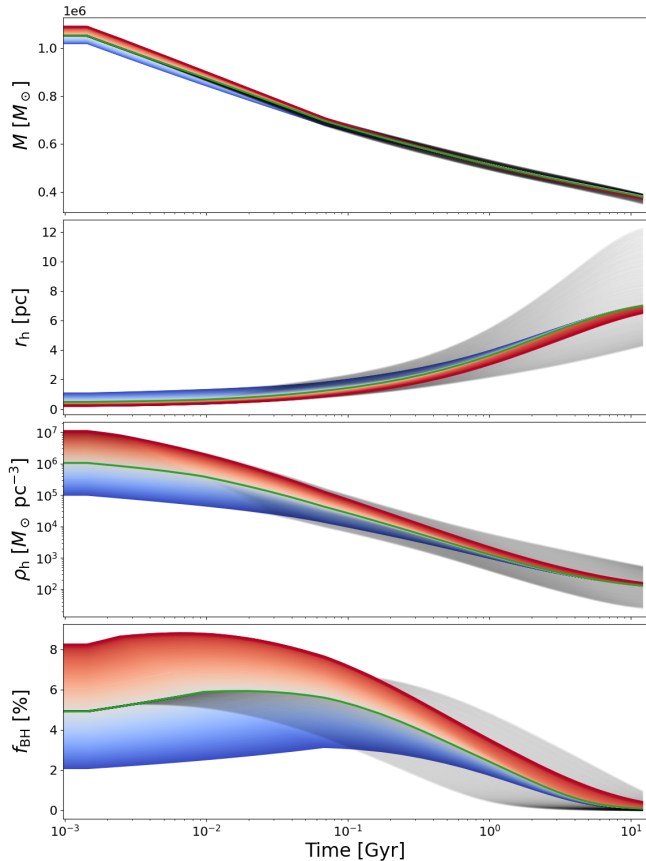


**Figure 13.** Evolution of cluster total mass, half-mass radius, half-mass density and BH mass fraction over time for a fiducial CLUSTERBH model with initial conditions  $M_0 = 1 \times 10^6 M_\odot$ ,  $\rho_{h,0} = 1 \times 10^6 M_\odot \text{pc}^{-3}$ ,  $[\text{Fe}/\text{H}] = -2$ ,  $R'_G = 5 \text{kpc}$ ,  $\alpha_1 = -0.82$  and  $\alpha_2 = -1.45$  (green line), as well as a set of models evolved from a grid of initial densities and corresponding BH natal kick strengths ( $f_k$ ) which result in similar present-day conditions (red to blue lines). The grey background lines represent models over the same grid of initial densities with a fixed  $f_k = 50\%$ , showing how their evolution differs under the same BH kick prescription.

demonstrates the existence of a clear degeneracy between the initial mass in BHs and the initial cluster density. It also shows that if the BH natal kicks are in reality stronger than commonly assumed, lower initial cluster densities may also be consistent with present-day observations. In a forthcoming paper we will harness the flexibility of our models to test this hypothesis in more detail by refitting our sample of clusters under different BH prescriptions and examining the impacts on the inferred initial conditions.

## 6. CONCLUSIONS

In this work, we have combined fast, evolutionary cluster models with multimass equilibrium models, providing a novel tool for the inference of the initial conditions of GCs from observations of their present-day structure and kinematics. We have validated these new coupled models and their ability to

recover both present-day and initial cluster conditions against mock observations of a large grid of CMC models. Finally we have applied them to a sample of 35 MW clusters, fitting to a number of observed proper motion, line-of-sight velocity, number density, and stellar mass function datasets, allowing us to explore the present-day stellar and remnant populations, and place constraints on their initial conditions. This has yielded a number of interesting conclusions:

1. We infer a distribution of initial half-mass densities across our sample which is notably high, peaking at  $\log_{10}(\rho_{h,0}) = 6.44^{+0.72}_{-1.03}$ , driven by typically very compact values of  $r_{h,0}$ .
2. In line with recent studies (e.g. D23; H. Baumgardt et al. 2023), we recover a stellar IMF which is *bottom-light* (i.e. deficient in low-mass stars) in comparison with canonical IMF prescriptions, with low-mass power-law slopes of  $\alpha_1 = 0.82^{+0.27}_{-0.20}$  and  $\alpha_2 = 1.47^{+0.45}_{-0.41}$ .
3. The majority of our GCs are consistent with having retained relatively small populations of BHs to the present day (typically less than  $f_{\text{BH}} = 1.5$  per cent), despite initially higher BH mass fractions, arising from our inferred IMF.
4. Despite the high inferred initial densities, many of our clusters are consistent with the recent density estimates of candidate proto-GCs at high redshifts, such as the COSMIC Gems clusters (A. Adamo et al. 2024).

These results, especially the notably high initial densities we infer, have important implications for many open fields of study, ranging from cluster formation to BH growth to GW sources.

These results may also be, however, particularly sensitive to the exact BH formation prescriptions assumed (e.g. their IFMRs and supernova kicks), and different assumptions could lead to remarkably different inferred initial conditions. While we adopt commonly assumed recipes here, these remain very uncertain and we have demonstrated that degeneracies exist between initial conditions and the initial BH mass fractions, which are in large part set by the adopted BH prescriptions. In a forthcoming work, we will investigate this problem in more detail by re-fitting our sample of clusters under a variety of different prescriptions for the BH natal kicks and IFMRs, and exploring whether, for example, stronger natal kicks allow for recovering the observed properties of these clusters with lower initial densities.

In addition, the distributions of initial conditions we present here represent only those of the individual clusters within our sample. To constrain the overall, shared, population-level distributions of initial conditions (e.g. the cluster mass function), accounting for the full MW GC population, including

dissolved and undetected clusters, would be required. In a future work, we will tackle this problem by applying our fast evolutionary models within a fully hierarchical Bayesian modelling framework.

#### ACKNOWLEDGEMENTS

ND is grateful for the support of the Durland Scholarship in Graduate Research and the MITACS Globalink Research Internship program, and for the hospitality of IC-CUB during the completion of this work. VHB acknowledges the support of the Natural Sciences and Engineering Research Council of Canada (NSERC) through grant RGPIN-2020-05990. FFP acknowledges the “la Caixa” Foundation (ID100010434) for financial support in the

form of a Doctoral INPhINIT fellowship (fellowship code LCF/BQ/DI23/11990067). MG acknowledges financial support from the grants PID2024-155720NB-I00, CEX2024-001451-M funded by MCIN/AEI/10.13039/501100011033 (State Agency for Research of the Spanish Ministry of Science and Innovation).

This research was enabled in part by support provided by ACENET ([www.ace-net.ca](http://www.ace-net.ca)) and the Digital Research Alliance of Canada (<https://alliancecan.ca>).

*Software:* `astropy` (Astropy Collaboration et al. 2018), `dynesty` (J. S. Speagle 2020; S. Koposov et al. 2025), `h5py` (A. Collette et al. 2022), `cmctoolkit` (N. Z. Rui et al. 2021b), `matplotlib` (J. D. Hunter 2007), `numpy` (C. R. Harris et al. 2020), `scipy` (P. Virtanen et al. 2020)

#### REFERENCES

- Adamo, A., Bradley, L. D., Vanzella, E., et al. 2024, *Nature*, 632, 513, doi: [10.1038/s41586-024-07703-7](https://doi.org/10.1038/s41586-024-07703-7)
- Alessandrini, E., Lanzoni, B., Ferraro, F. R., Mocchi, P., & Vesperini, E. 2016, *The Astrophysical Journal*, 833, 252, doi: [10.3847/1538-4357/833/2/252](https://doi.org/10.3847/1538-4357/833/2/252)
- Alexander, P. E. R., & Gieles, M. 2012, *Monthly Notices of the Royal Astronomical Society*, 422, 3415, doi: [10.1111/j.1365-2966.2012.20867.x](https://doi.org/10.1111/j.1365-2966.2012.20867.x)
- Alexander, P. E. R., Gieles, M., Lamers, H. J. G. L. M., & Baumgardt, H. 2014, *Monthly Notices of the Royal Astronomical Society*, 442, 1265, doi: [10.1093/mnras/stu899](https://doi.org/10.1093/mnras/stu899)
- Antonini, F., & Gieles, M. 2020a, 492, 2936, doi: [10.1093/mnras/stz3584](https://doi.org/10.1093/mnras/stz3584)
- Antonini, F., & Gieles, M. 2020b, 102, 123016, doi: [10.1103/PhysRevD.102.123016](https://doi.org/10.1103/PhysRevD.102.123016)
- Antonini, F., Gieles, M., Dosopoulou, F., & Chattopadhyay, D. 2023, 522, 466, doi: [10.1093/mnras/stad972](https://doi.org/10.1093/mnras/stad972)
- Antonini, F., Gieles, M., & Gualandris, A. 2019, *Monthly Notices of the Royal Astronomical Society*, 486, 5008, doi: [10.1093/mnras/stz1149](https://doi.org/10.1093/mnras/stz1149)
- Antonini, F., & Rasio, F. A. 2016, 831, 187, doi: [10.3847/0004-637X/831/2/187](https://doi.org/10.3847/0004-637X/831/2/187)
- Arca Sedda, M., Askar, A., & Giersz, M. 2018, 479, 4652, doi: [10.1093/mnras/sty1859](https://doi.org/10.1093/mnras/sty1859)
- Arca Sedda, M., Kamlah, A. W. H., Spurzem, R., et al. 2024, 528, 5119, doi: [10.1093/mnras/stad3952](https://doi.org/10.1093/mnras/stad3952)
- Askar, A., Arca Sedda, M., & Giersz, M. 2018, 478, 1844, doi: [10.1093/mnras/sty1186](https://doi.org/10.1093/mnras/sty1186)
- Astropy Collaboration, Price-Whelan, A. M., Sipőcz, B. M., et al. 2018, 156, 123, doi: [10.3847/1538-3881/aabc4f](https://doi.org/10.3847/1538-3881/aabc4f)
- Atri, P., Miller-Jones, J. C. A., Bahramian, A., et al. 2019, *Monthly Notices of the Royal Astronomical Society*, 489, 3116, doi: [10.1093/mnras/stz2335](https://doi.org/10.1093/mnras/stz2335)
- Balbinot, E., & Gieles, M. 2018, *Monthly Notices of the Royal Astronomical Society*, 474, 2479, doi: [10.1093/mnras/stx2708](https://doi.org/10.1093/mnras/stx2708)
- Banerjee, S., Belczynski, K., Fryer, C. L., et al. 2020, 639, A41, doi: [10.1051/0004-6361/201935332](https://doi.org/10.1051/0004-6361/201935332)
- Bastian, N., & Lardo, C. 2018, 56, 83, doi: [10.1146/annurev-astro-081817-051839](https://doi.org/10.1146/annurev-astro-081817-051839)
- Baumgardt, H. 2017, 464, 2174, doi: [10.1093/mnras/stw2488](https://doi.org/10.1093/mnras/stw2488)
- Baumgardt, H., Hénault-Brunet, V., Dickson, N., & Sollima, A. 2023, 521, 3991, doi: [10.1093/mnras/stad631](https://doi.org/10.1093/mnras/stad631)
- Baumgardt, H., & Hilker, M. 2018, 478, 1520, doi: [10.1093/mnras/sty1057](https://doi.org/10.1093/mnras/sty1057)
- Baumgardt, H., Hilker, M., Sollima, A., & Bellini, A. 2019, 482, 5138, doi: [10.1093/mnras/sty2997](https://doi.org/10.1093/mnras/sty2997)
- Baumgardt, H., & Makino, J. 2003, *Monthly Notices of the Royal Astronomical Society*, 340, 227, doi: [10.1046/j.1365-8711.2003.06286.x](https://doi.org/10.1046/j.1365-8711.2003.06286.x)
- Baumgardt, H., & Vasiliev, E. 2021, 505, 5957, doi: [10.1093/mnras/stab1474](https://doi.org/10.1093/mnras/stab1474)
- Bekki, K., & Freeman, K. C. 2003, 346, L11, doi: [10.1046/j.1365-2966.2003.07275.x](https://doi.org/10.1046/j.1365-2966.2003.07275.x)
- Belczynski, K., Heger, A., Gladysz, W., et al. 2016, *Astronomy and Astrophysics*, 594, A97, doi: [10.1051/0004-6361/201628980](https://doi.org/10.1051/0004-6361/201628980)
- Bianchini, P., Varri, A. L., Askar, A., Marklund, A., & Mastrobuono-Battisti, A. 2026, 708, A10, doi: [10.1051/0004-6361/202557909](https://doi.org/10.1051/0004-6361/202557909)
- Bocchi, V., Liempi, M., & Schleicher, D. R. G. 2026, arXiv e-prints, arXiv:2605.20381, doi: [10.48550/arXiv.2605.20381](https://doi.org/10.48550/arXiv.2605.20381)
- Bocchioli, L., & Fragione, G. 2024, 110, 023007, doi: [10.1103/PhysRevD.110.023007](https://doi.org/10.1103/PhysRevD.110.023007)
- Breen, P. G., & Heggge, D. C. 2013, *Monthly Notices of the Royal Astronomical Society*, 432, 2779, doi: [10.1093/mnras/stt628](https://doi.org/10.1093/mnras/stt628)
- Cai, M. X., Gieles, M., Heggge, D. C., & Varri, A. L. 2016, 455, 596, doi: [10.1093/mnras/stv2325](https://doi.org/10.1093/mnras/stv2325)

- Casertano, S., & Hut, P. 1985, *The Astrophysical Journal*, 298, 80, doi: [10.1086/163589](https://doi.org/10.1086/163589)
- Chatterjee, S., Umbreit, S., Fregeau, J. M., & Rasio, F. A. 2013, 429, 2881, doi: [10.1093/mnras/sts464](https://doi.org/10.1093/mnras/sts464)
- Chattopadhyay, D., Marín Pina, D., Gieles, M., Antonini, F., & Fronimos Pouliasis, F. 2026, arXiv e-prints, arXiv:2604.09773, doi: [10.48550/arXiv.2604.09773](https://doi.org/10.48550/arXiv.2604.09773)
- Choi, J., Dotter, A., Conroy, C., et al. 2016, 823, 102, doi: [10.3847/0004-637X/823/2/102](https://doi.org/10.3847/0004-637X/823/2/102)
- Claeyssens, A., Adamo, A., Richard, J., et al. 2023, *Monthly Notices of the Royal Astronomical Society*, 520, 2180, doi: [10.1093/mnras/stac3791](https://doi.org/10.1093/mnras/stac3791)
- Claeyssens, A., Adamo, A., Kokorev, V., et al. 2026, arXiv, doi: [10.48550/arXiv.2601.16281](https://doi.org/10.48550/arXiv.2601.16281)
- Collette, A., Kluyver, T., Caswell, T. A., et al. 2022., 3.7.0 Zenodo, doi: [10.5281/zenodo.6575970](https://doi.org/10.5281/zenodo.6575970)
- Cournoyer-Cloutier, C., Sills, A., Harris, W. E., et al. 2024, 977, 203, doi: [10.3847/1538-4357/ad90b3](https://doi.org/10.3847/1538-4357/ad90b3)
- Crocker, R. M., Krumholz, M. R., Thompson, T. A., Baumgardt, H., & Mackey, D. 2018, *Monthly Notices of the Royal Astronomical Society*, 481, 4895, doi: [10.1093/mnras/sty2659](https://doi.org/10.1093/mnras/sty2659)
- Dalgleish, H., Kamann, S., Usher, C., et al. 2020, 492, 3859, doi: [10.1093/mnras/staa091](https://doi.org/10.1093/mnras/staa091)
- De Angeli, F., Piotto, G., Cassisi, S., et al. 2005, 130, 116, doi: [10.1086/430723](https://doi.org/10.1086/430723)
- de Boer, T. J. L., Gieles, M., Balbinot, E., et al. 2019, 485, 4906, doi: [10.1093/mnras/stz651](https://doi.org/10.1093/mnras/stz651)
- den Brok, M., van de Ven, G., van den Bosch, R., & Watkins, L. 2014, 438, 487, doi: [10.1093/mnras/stt2221](https://doi.org/10.1093/mnras/stt2221)
- Dickson, N., Hénault-Brunet, V., Baumgardt, H., Gieles, M., & Smith, P. J. 2023, 522, 5320, doi: [10.1093/mnras/stad1254](https://doi.org/10.1093/mnras/stad1254)
- Dickson, N., Smith, P. J., Hénault-Brunet, V., Gieles, M., & Baumgardt, H. 2024, 529, 331, doi: [10.1093/mnras/stae470](https://doi.org/10.1093/mnras/stae470)
- Disberg, P., & Mandel, I. 2025, *The Astrophysical Journal*, 989, L8, doi: [10.3847/2041-8213/adf286](https://doi.org/10.3847/2041-8213/adf286)
- Dotter, A. 2016, 222, 8, doi: [10.3847/0067-0049/222/1/8](https://doi.org/10.3847/0067-0049/222/1/8)
- Dotter, A., Chaboyer, B., Jevremović, D., et al. 2007, 134, 376, doi: [10.1086/517915](https://doi.org/10.1086/517915)
- Dotter, A., Chaboyer, B., Jevremović, D., et al. 2008, 178, 89, doi: [10.1086/589654](https://doi.org/10.1086/589654)
- Forbes, D. A., Bastian, N., Gieles, M., et al. 2018, *Proceedings of the Royal Society of London Series A*, 474, 20170616, doi: [10.1098/rspa.2017.0616](https://doi.org/10.1098/rspa.2017.0616)
- Fregeau, J. M., Cheung, P., Portegies Zwart, S. F., & Rasio, F. A. 2004, 352, 1, doi: [10.1111/j.1365-2966.2004.07914.x](https://doi.org/10.1111/j.1365-2966.2004.07914.x)
- Fronimos Pouliasis, F., Dickson, N., Marín Pina, D., et al. 2026, arXiv e-prints, arXiv:2605.28088, <https://arxiv.org/abs/2605.28088>
- Fryer, C. L., Belczynski, K., Wiktorowicz, G., et al. 2012, 749, 91, doi: [10.1088/0004-637X/749/1/91](https://doi.org/10.1088/0004-637X/749/1/91)
- Fujii, M. S., Wang, L., Tanikawa, A., Hirai, Y., & Saitoh, T. R. 2024, *Science*, 384, 1488, doi: [10.1126/science.adi4211](https://doi.org/10.1126/science.adi4211)
- Gaia Collaboration, Vallenari, A., Brown, A. G. A., et al. 2023, 674, A1, doi: [10.1051/0004-6361/202243940](https://doi.org/10.1051/0004-6361/202243940)
- Gaia Collaboration, Panuzzo, P., Mazeh, T., et al. 2024, arXiv e-prints, arXiv:2404.10486, doi: [10.48550/arXiv.2404.10486](https://doi.org/10.48550/arXiv.2404.10486)
- Gieles, M., Alexander, P. E. R., Lamers, H. J. G. L. M., & Baumgardt, H. 2014, *Monthly Notices of the Royal Astronomical Society*, 437, 916, doi: [10.1093/mnras/stt1980](https://doi.org/10.1093/mnras/stt1980)
- Gieles, M., Heggie, D. C., & Zhao, H. 2011, *Monthly Notices of the Royal Astronomical Society*, 413, 2509, doi: [10.1111/j.1365-2966.2011.18320.x](https://doi.org/10.1111/j.1365-2966.2011.18320.x)
- Gieles, M., Padoan, P., Charbonnel, C., Vink, J. S., & Ramírez-Galeano, L. 2025, 544, 483, doi: [10.1093/mnras/staf1314](https://doi.org/10.1093/mnras/staf1314)
- Gieles, M., & Zocchi, A. 2015, 454, 576, doi: [10.1093/mnras/stv1848](https://doi.org/10.1093/mnras/stv1848)
- Giersz, M., & Heggie, D. C. 2009, 395, 1173, doi: [10.1111/j.1365-2966.2009.14638.x](https://doi.org/10.1111/j.1365-2966.2009.14638.x)
- Giersz, M., Heggie, D. C., Hurley, J. R., & Hypki, A. 2013, *Monthly Notices of the Royal Astronomical Society*, 431, 2184, doi: [10.1093/mnras/stt307](https://doi.org/10.1093/mnras/stt307)
- Giesers, B., Dreizler, S., Husser, T.-O., et al. 2018, 475, L15, doi: [10.1093/mnras/lsx203](https://doi.org/10.1093/mnras/lsx203)
- Giesers, B., Kamann, S., Dreizler, S., et al. 2019, 632, A3, doi: [10.1051/0004-6361/201936203](https://doi.org/10.1051/0004-6361/201936203)
- Grudić, M. Y., Hopkins, P. F., Quataert, E., & Murray, N. 2019, *Monthly Notices of the Royal Astronomical Society*, 483, 5548, doi: [10.1093/mnras/sty3386](https://doi.org/10.1093/mnras/sty3386)
- Häberle, M., Neumayer, N., Seth, A., et al. 2024, *Nature*, 631, 285, doi: [10.1038/s41586-024-07511-z](https://doi.org/10.1038/s41586-024-07511-z)
- Häberle, M., Neumayer, N., Clontz, C., et al. 2025, 983, 95, doi: [10.3847/1538-4357/adbe67](https://doi.org/10.3847/1538-4357/adbe67)
- Harris, C. R., Millman, K. J., van der Walt, S. J., et al. 2020, 585, 357, doi: [10.1038/s41586-020-2649-2](https://doi.org/10.1038/s41586-020-2649-2)
- Harris, W. E. 1996, 112, 1487, doi: [10.1086/118116](https://doi.org/10.1086/118116)
- Heggie, D., & Hut, P. 2003, *The Gravitational Million-Body Problem: A Multidisciplinary Approach to Star Cluster Dynamics*
- Heggie, D. C., & Giersz, M. 2008, 389, 1858, doi: [10.1111/j.1365-2966.2008.13702.x](https://doi.org/10.1111/j.1365-2966.2008.13702.x)
- Hénault-Brunet, V., Gieles, M., Sollima, A., et al. 2019, 483, 1400, doi: [10.1093/mnras/sty3187](https://doi.org/10.1093/mnras/sty3187)
- Hénault-Brunet, V., Gieles, M., Strader, J., et al. 2020, 491, 113, doi: [10.1093/mnras/stz2995](https://doi.org/10.1093/mnras/stz2995)
- Hénon, M. 1961, *Annales d'Astrophysique*, 24, 369
- Hénon, M. 1965, *Annales d'Astrophysique*, 28, 62
- Hénon, M. 1971a, *Astrophysics and Space Science*, 13, 284, doi: [10.1007/BF00649159](https://doi.org/10.1007/BF00649159)

- Hénon, M. 1971b, *Astrophysics and Space Science*, 14, 151, doi: [10.1007/BF00649201](https://doi.org/10.1007/BF00649201)
- Hénon, M. 1975, in *Dynamics of Stellar Systems*, Vol. 69, 133
- Hobbs, G., Lorimer, D. R., Lyne, A. G., & Kramer, M. 2005, 360, 974, doi: [10.1111/j.1365-2966.2005.09087.x](https://doi.org/10.1111/j.1365-2966.2005.09087.x)
- Hopkins, P. F., Murray, N., Quataert, E., & Thompson, T. A. 2010, 401, L19, doi: [10.1111/j.1745-3933.2009.00777.x](https://doi.org/10.1111/j.1745-3933.2009.00777.x)
- Hunter, J. D. 2007, *Computing in Science and Engineering*, 9, 90, doi: [10.1109/MCSE.2007.55](https://doi.org/10.1109/MCSE.2007.55)
- Hypki, A., & Giersz, M. 2013, *Monthly Notices of the Royal Astronomical Society*, 429, 1221, doi: [10.1093/mnras/sts415](https://doi.org/10.1093/mnras/sts415)
- Kacharov, N., Bianchini, P., Koch, A., et al. 2014, 567, A69, doi: [10.1051/0004-6361/201423709](https://doi.org/10.1051/0004-6361/201423709)
- Kamann, S., Husser, T. O., Dreizler, S., et al. 2018, 473, 5591, doi: [10.1093/mnras/stx2719](https://doi.org/10.1093/mnras/stx2719)
- King, I. R. 1966, *The Astronomical Journal*, 71, 64, doi: [10.1086/109857](https://doi.org/10.1086/109857)
- Koposov, S., Speagle, J., Barbary, K., et al. 2025., v3.0.0 Zenodo, doi: [10.5281/zenodo.17268284](https://doi.org/10.5281/zenodo.17268284)
- Kremer, K., Chatterjee, S., Ye, C. S., Rodriguez, C. L., & Rasio, F. A. 2019, *The Astrophysical Journal*, 871, 38, doi: [10.3847/1538-4357/aaf646](https://doi.org/10.3847/1538-4357/aaf646)
- Kremer, K., Weatherford, N. C., Hopkins, P. F., Rui, N. Z., & Ye, C. S. 2025, *The Astrophysical Journal*, 993, L34, doi: [10.3847/2041-8213/ae1233](https://doi.org/10.3847/2041-8213/ae1233)
- Kremer, K., Ye, C. S., Chatterjee, S., Rodriguez, C. L., & Rasio, F. A. 2020a, in *Star Clusters: From the Milky Way to the Early Universe*, ed. A. Bragaglia, M. Davies, A. Sills, & E. Vesperini, Vol. 351, 357–366, doi: [10.1017/S1743921319007269](https://doi.org/10.1017/S1743921319007269)
- Kremer, K., Ye, C. S., Rui, N. Z., et al. 2020b, 247, 48, doi: [10.3847/1538-4365/ab7919](https://doi.org/10.3847/1538-4365/ab7919)
- Kritos, K., Stokov, V., Baibhav, V., & Berti, E. 2024, 110, 043023, doi: [10.1103/PhysRevD.110.043023](https://doi.org/10.1103/PhysRevD.110.043023)
- Kroupa, P. 2001, 322, 231, doi: [10.1046/j.1365-8711.2001.04022.x](https://doi.org/10.1046/j.1365-8711.2001.04022.x)
- Krujssens, J. M. D. 2026, in *Encyclopedia of Astrophysics*, Volume 4, Vol. 4, eprint: [arXiv:2501.16438](https://arxiv.org/abs/2501.16438), 500–534, doi: [10.1016/B978-0-443-21439-4.00078-X](https://doi.org/10.1016/B978-0-443-21439-4.00078-X)
- Krumholz, M. R., McKee, C. F., & Bland-Hawthorn, J. 2019, *Annual Review of Astronomy and Astrophysics*, 57, 227, doi: [10.1146/annurev-astro-091918-104430](https://doi.org/10.1146/annurev-astro-091918-104430)
- Lahén, N., Naab, T., Rantala, A., & Partmann, C. 2025a, *Monthly Notices of the Royal Astronomical Society*, 543, 1023, doi: [10.1093/mnras/staf1546](https://doi.org/10.1093/mnras/staf1546)
- Lahén, N., Rantala, A., Naab, T., et al. 2025b, *Monthly Notices of the Royal Astronomical Society*, 538, 2129, doi: [10.1093/mnras/staf350](https://doi.org/10.1093/mnras/staf350)
- Lamers, H. J. G. L. M., Baumgardt, H., & Gieles, M. 2013, *Monthly Notices of the Royal Astronomical Society*, 433, 1378, doi: [10.1093/mnras/stt808](https://doi.org/10.1093/mnras/stt808)
- Libralato, M., Bellini, A., Vesperini, E., et al. 2022, 934, 150, doi: [10.3847/1538-4357/ac7727](https://doi.org/10.3847/1538-4357/ac7727)
- Libralato, M., Gerasimov, R., Bedin, L., et al. 2024, *Astronomy and Astrophysics*, 690, A371, doi: [10.1051/0004-6361/202451295](https://doi.org/10.1051/0004-6361/202451295)
- Lützgendorf, N., Kissler-Patig, M., Gebhardt, K., et al. 2013, 552, A49, doi: [10.1051/0004-6361/201220307](https://doi.org/10.1051/0004-6361/201220307)
- Mai, A., Kremer, K., & Kiroğlu, F. 2026, *The Astrophysical Journal*, 998, 138, doi: [10.3847/1538-4357/ae2de5](https://doi.org/10.3847/1538-4357/ae2de5)
- Mandel, I. 2016, 456, 578, doi: [10.1093/mnras/stv2733](https://doi.org/10.1093/mnras/stv2733)
- Mapelli, M., Dall’Amico, M., Bouffanais, Y., et al. 2021, 505, 339, doi: [10.1093/mnras/stab1334](https://doi.org/10.1093/mnras/stab1334)
- Marín-Franch, A., Aparicio, A., Piotto, G., et al. 2009, 694, 1498, doi: [10.1088/0004-637X/694/2/1498](https://doi.org/10.1088/0004-637X/694/2/1498)
- McNamara, B. J., Harrison, T. E., Baumgardt, H., & Khalaj, P. 2012, 745, 175, doi: [10.1088/0004-637X/745/2/175](https://doi.org/10.1088/0004-637X/745/2/175)
- Melbourne, J., Sarajedini, A., Layden, A., & Martins, D. H. 2000, 120, 3127, doi: [10.1086/316869](https://doi.org/10.1086/316869)
- Meza, A., Navarro, J. F., Abadi, M. G., & Steinmetz, M. 2005, 359, 93, doi: [10.1111/j.1365-2966.2005.08869.x](https://doi.org/10.1111/j.1365-2966.2005.08869.x)
- Michie, R. W. 1962, *Monthly Notices of the Royal Astronomical Society*, 125, 127, doi: [10.1093/mnras/125.2.127](https://doi.org/10.1093/mnras/125.2.127)
- Miocchi, P., Lanzoni, B., Ferraro, F. R., et al. 2013, 774, 151, doi: [10.1088/0004-637X/774/2/151](https://doi.org/10.1088/0004-637X/774/2/151)
- Morscher, M., Pattabiraman, B., Rodriguez, C., Rasio, F. A., & Umbreit, S. 2015, 800, 9, doi: [10.1088/0004-637X/800/1/9](https://doi.org/10.1088/0004-637X/800/1/9)
- Paduano, A., Bahramian, A., Miller-Jones, J. C. A., et al. 2024, 961, 54, doi: [10.3847/1538-4357/ad0e68](https://doi.org/10.3847/1538-4357/ad0e68)
- Peuten, M., Zocchi, A., Gieles, M., & Hénault-Brunet, V. 2017, 470, 2736, doi: [10.1093/mnras/stx1311](https://doi.org/10.1093/mnras/stx1311)
- Pfahl, E., Rappaport, S., & Podsiadlowski, P. 2002, 573, 283, doi: [10.1086/340494](https://doi.org/10.1086/340494)
- Polak, B., Mac Low, M.-M., Klessen, R. S., et al. 2024, 690, A94, doi: [10.1051/0004-6361/202348840](https://doi.org/10.1051/0004-6361/202348840)
- Popov, S., Müller, B., & Mandel, I. 2025, 101, 101734, doi: [10.1016/j.newar.2025.101734](https://doi.org/10.1016/j.newar.2025.101734)
- Portegies Zwart, S. F., Baumgardt, H., Hut, P., Makino, J., & McMillan, S. L. W. 2004, 428, 724, doi: [10.1038/nature02448](https://doi.org/10.1038/nature02448)
- Portegies Zwart, S. F., & McMillan, S. L. W. 2002, 576, 899, doi: [10.1086/341798](https://doi.org/10.1086/341798)
- Portegies Zwart, S. F., McMillan, S. L. W., & Gieles, M. 2010, *Annual Review of Astronomy and Astrophysics*, 48, 431, doi: [10.1146/annurev-astro-081309-130834](https://doi.org/10.1146/annurev-astro-081309-130834)
- Ramírez-Galeano, L., Charbonnel, C., Fragos, T., et al. 2025, 699, A223, doi: [10.1051/0004-6361/202453462](https://doi.org/10.1051/0004-6361/202453462)
- Rantala, A., Naab, T., Lahén, N., et al. 2026, *Monthly Notices of the Royal Astronomical Society*, 549, stag986, doi: [10.1093/mnras/stag986](https://doi.org/10.1093/mnras/stag986)
- Reina-Campos, M., Gnedin, O. Y., Sills, A., & Li, H. 2025, 978, 15, doi: [10.3847/1538-4357/ad909f](https://doi.org/10.3847/1538-4357/ad909f)

- Repetto, S., Igoshev, A. P., & Nelemans, G. 2017, *Monthly Notices of the Royal Astronomical Society*, 467, 298, doi: [10.1093/mnras/stx027](https://doi.org/10.1093/mnras/stx027)
- Rodriguez, C. L., Amaro-Seoane, P., Chatterjee, S., et al. 2018, 98, 123005, doi: [10.1103/PhysRevD.98.123005](https://doi.org/10.1103/PhysRevD.98.123005)
- Rodriguez, C. L., Chatterjee, S., & Rasio, F. A. 2016, 93, 084029, doi: [10.1103/PhysRevD.93.084029](https://doi.org/10.1103/PhysRevD.93.084029)
- Rodriguez, C. L., Weatherford, N. C., Coughlin, S. C., et al. 2022, 258, 22, doi: [10.3847/1538-4365/ac2edf](https://doi.org/10.3847/1538-4365/ac2edf)
- Roman-Garza, J., Fragos, T., Charbonnel, C., et al. 2026, 707, A163, doi: [10.1051/0004-6361/202557899](https://doi.org/10.1051/0004-6361/202557899)
- Rui, N. Z., Kremer, K., Weatherford, N. C., et al. 2021a, 912, 102, doi: [10.3847/1538-4357/abed49](https://doi.org/10.3847/1538-4357/abed49)
- Rui, N. Z., Kremer, K., Weatherford, N. C., et al. 2021b., 1.0 Zenodo, doi: [10.5281/zenodo.4579951](https://doi.org/10.5281/zenodo.4579951)
- Sarajedini, A., Bedin, L. R., Chaboyer, B., et al. 2007, 133, 1658, doi: [10.1086/511979](https://doi.org/10.1086/511979)
- Sharma, K., & Rodriguez, C. L. 2025, 983, 162, doi: [10.3847/1538-4357/adbbdf](https://doi.org/10.3847/1538-4357/adbbdf)
- Speagle, J. S. 2020, 493, 3132, doi: [10.1093/mnras/staa278](https://doi.org/10.1093/mnras/staa278)
- Spitzer, L. S. 1987, *Dynamical Evolution of Globular Clusters* (Princeton University Press)
- Strader, J., Chomiuk, L., Maccarone, T. J., Miller-Jones, J. C. A., & Seth, A. C. 2012, 490, 71, doi: [10.1038/nature11490](https://doi.org/10.1038/nature11490)
- The LIGO Scientific Collaboration, the Virgo Collaboration, & the KAGRA Collaboration. 2026, arXiv e-prints, arXiv:2605.27226, doi: [10.48550/arXiv.2605.27226](https://doi.org/10.48550/arXiv.2605.27226)
- Torniamenti, S., Hoyer, N., Neumayer, N., Smith, P. J., & Arca Sedda, M. 2026, arXiv e-prints, arXiv:2606.14852, doi: [10.48550/arXiv.2606.14852](https://doi.org/10.48550/arXiv.2606.14852)
- Trager, S. C., King, I. R., & Djorgovski, S. 1995, 109, 218, doi: [10.1086/117268](https://doi.org/10.1086/117268)
- Tremou, E., Strader, J., Chomiuk, L., et al. 2018, 862, 16, doi: [10.3847/1538-4357/aac9b9](https://doi.org/10.3847/1538-4357/aac9b9)
- VandenBerg, D. A., Brogaard, K., Leaman, R., & Casagrande, L. 2013, 775, 134, doi: [10.1088/0004-637X/775/2/134](https://doi.org/10.1088/0004-637X/775/2/134)
- Vanzella, E., Claeysens, A., Welch, B., et al. 2023, *The Astrophysical Journal*, 945, 53, doi: [10.3847/1538-4357/acb59a](https://doi.org/10.3847/1538-4357/acb59a)
- Vasiliev, E., & Baumgardt, H. 2021, 505, 5978, doi: [10.1093/mnras/stab1475](https://doi.org/10.1093/mnras/stab1475)
- Vergara, M. C., Askar, A., Flammini Dotti, F., et al. 2026, 707, A71, doi: [10.1051/0004-6361/202556878](https://doi.org/10.1051/0004-6361/202556878)
- Virtanen, P., Gommers, R., Oliphant, T. E., et al. 2020, *Nature Methods*, 17, 261, doi: [10.1038/s41592-019-0686-2](https://doi.org/10.1038/s41592-019-0686-2)
- Vital, E., Kremer, K., Libralato, M., Mamon, G. A., & Bellini, A. 2022, 514, 806, doi: [10.1093/mnras/stac1337](https://doi.org/10.1093/mnras/stac1337)
- Vital, E., Libralato, M., Kremer, K., et al. 2023, 522, 5740, doi: [10.1093/mnras/stad1068](https://doi.org/10.1093/mnras/stad1068)
- Wang, L., Spurzem, R., Aarseth, S., et al. 2016, 458, 1450, doi: [10.1093/mnras/stw274](https://doi.org/10.1093/mnras/stw274)
- Watkins, L. L., van der Marel, R. P., Bellini, A., & Anderson, J. 2015, 803, 29, doi: [10.1088/0004-637X/803/1/29](https://doi.org/10.1088/0004-637X/803/1/29)
- Weatherford, N. C., Chatterjee, S., Kremer, K., & Rasio, F. A. 2020, 898, 162, doi: [10.3847/1538-4357/ab9f98](https://doi.org/10.3847/1538-4357/ab9f98)
- Weatherford, N. C., Chatterjee, S., Rodriguez, C. L., & Rasio, F. A. 2018, 864, 13, doi: [10.3847/1538-4357/aad63d](https://doi.org/10.3847/1538-4357/aad63d)
- Whitaker, M., Kerr, E., Seth, A., et al. 2026, arXiv e-prints, arXiv:2606.18350. <https://arxiv.org/abs/2606.18350>
- Willcox, R., Marchant, P., Vigna-Gómez, A., et al. 2025a, 700, A59, doi: [10.1051/0004-6361/202555274](https://doi.org/10.1051/0004-6361/202555274)
- Willcox, R., Schneider, F. R. N., Laplace, E., et al. 2025b, arXiv e-prints, arXiv:2510.07573, doi: [10.48550/arXiv.2510.07573](https://doi.org/10.48550/arXiv.2510.07573)
- Williams, C. E., Naoz, S., Lake, W., et al. 2025, 990, 135, doi: [10.3847/1538-4357/adf19d](https://doi.org/10.3847/1538-4357/adf19d)
- Zocchi, A., Gieles, M., & Hénault-Brunet, V. 2019, 482, 4713, doi: [10.1093/mnras/sty1508](https://doi.org/10.1093/mnras/sty1508)

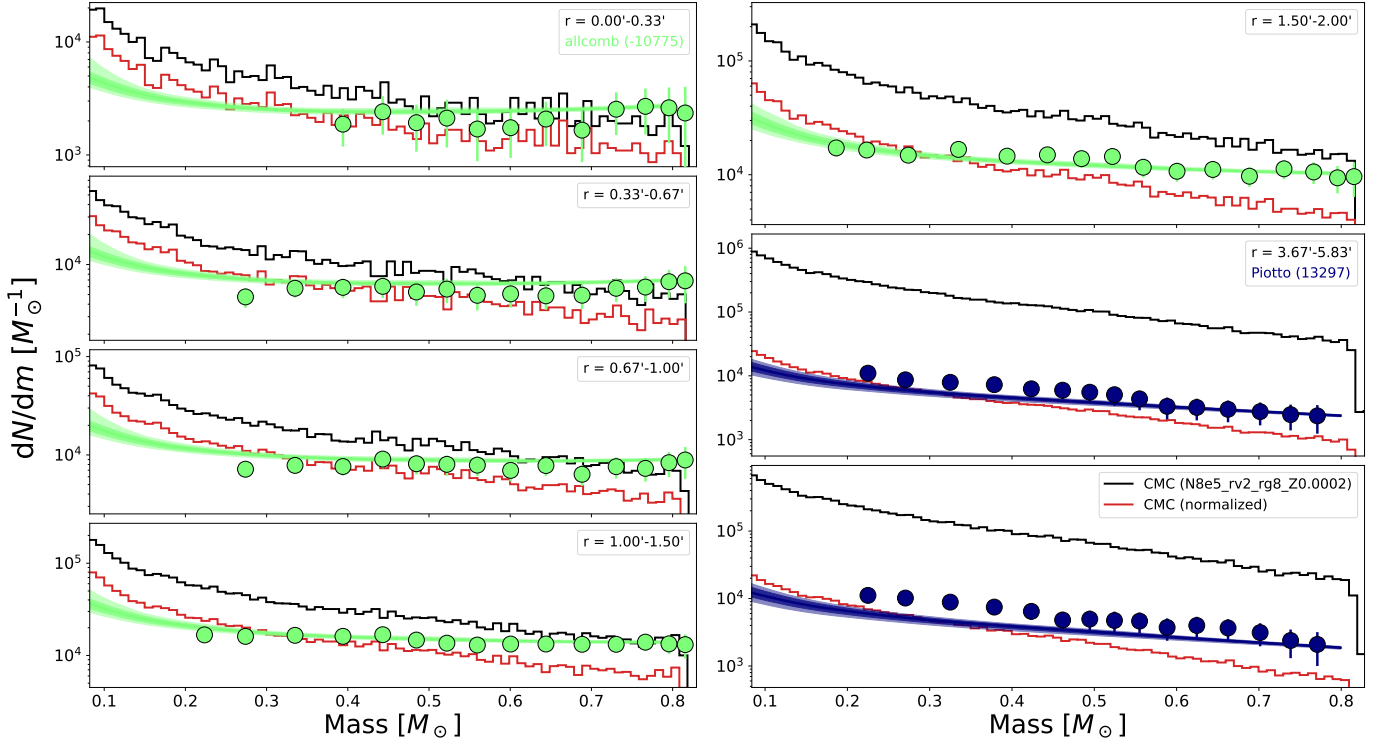


**Figure 14.** Comparison of the present-day local stellar mass functions between our fit to NGC 3201 and the CMC model best matching the velocity dispersion and surface brightness profile of the cluster ( $N_0 = 8 \times 10^5$ ,  $r_{v,0} = 2$  pc,  $R_g = 8$  kpc and  $Z = 0.0002$ ) (K. Kremer et al. 2019; N. Z. Rui et al. 2021a). Each panel shows the number of stars per unit mass as a function of stellar mass, for different projected distance ranges from the cluster centre. The dark and light shaded regions represent the  $1\sigma$  and  $2\sigma$  credible intervals of the model fits, respectively. The measurements used to constrain the models are shown alongside their  $1\sigma$  uncertainties by the circles and errorbars. The original CMC snapshot mass functions are shown in black. In red, the same CMC mass functions are scaled to align with our fits, in order to highlight the difference in slope between the two.

## APPENDIX

### A. ALL FIT PARAMETERS

### B. CMC MASS FUNCTION COMPARISON

To demonstrate the origin of the IMF we infer (Section 4.4), in Figure 14 we compare our fits to an example cluster (NGC 3201) with the best-matching CMC model of this cluster. For this comparison, we use the CMC snapshot that has been used in previous studies to represent NGC 3201 (e.g. K. Kremer et al. 2019; E. Vitral et al. 2022), based on matching the CMC snapshots to the observed surface brightness and velocity dispersion profiles (N. Z. Rui et al. 2021a)<sup>16</sup>. We also overplot, in red, the same CMC mass function scaled to match the mass functions of our best-fitting model within each panel, in order to more easily compare the slope of the mass function, irrespective of the total number of stars, which could likely be improved by choosing a lower-mass CMC model.

It is clearly seen in Figure 14 that the CMC snapshot, which has been previously shown to match the density and kinematic data of NGC 3201 well, is unable to reproduce the mass function data. The slopes of these local mass functions (and of the the global mass function) in CMC are too steep, and lead to too many low-mass stars. This is the direct consequence of the P. Kroupa (2001) IMF assumed in the CMC grid. The present-day mass function datasets place useful constraints on the IMF, and are largely the reason we infer a bottom-light IMF across our sample. It would be valuable, in the future, to compute a similar grid of CMC

<sup>16</sup> N. Z. Rui et al. (2021a) also note that the same CMC model but with  $N_0 = 4 \times 10^5 M_\odot$  is also a good match under their methodology, but the differences shown here remain similar, and thus we opt to show the snapshot which is used in other studies.

Cluster	$\hat{\phi}_0$	$M_0 [10^6 M_\odot]$	$r_{h,0}$ [pc]	$\log(\hat{r}_a)$	$g$	$s^2$ [arcmin $^{-4}$ ]	$F$	$\alpha_1$	$\alpha_2$	$d$ [kpc]	$\delta$	$\zeta$	$\eta$
NGC 104	15.3 $^{+0.4}_{-0.4}$	1.87 $^{+0.06}_{-0.04}$	0.59 $^{+0.04}_{-0.05}$	5.7 $_{-0.9}^{+1.4}$	1.55 $^{+0.03}_{-0.04}$	0.02 $^{+0.03}_{-0.01}$	4.6 $^{+0.1}_{-0.1}$	0.64 $^{+0.05}_{-0.05}$	2.10 $^{+0.08}_{-0.10}$	4.42 $^{+0.01}_{-0.02}$	0.153 $^{+0.007}_{-0.007}$	0.87 $^{+0.04}_{-0.03}$	3.0 $^{+0.0}_{-0.6}$
NGC 362*	53 $^{\dagger}$	0.98 $^{+0.02}_{-0.02}$	0.24 $^{+0.01}_{-0.01}$	0.8 $^{+0.2}_{-0.1}$	1.67 $^{+0.06}_{-0.08}$	0.00015 $^{+0.00009}_{-0.00005}$	2.6 $^{+0.2}_{-0.2}$	1.06 $^{+0.04}_{-0.05}$	1.56 $^{+0.06}_{-0.08}$	9.13 $^{+0.06}_{-0.07}$	0.44 $^{+0.02}_{-0.02}$	0.96 $^{+0.03}_{-0.06}$	-1.3 $^{+0.2}_{-0.1}$
NGC 1261	59 $^{\dagger}$	0.53 $^{+0.01}_{-0.01}$	0.44 $^{+0.02}_{-0.02}$	0.3 $^{+0.1}_{-0.1}$	2.22 $^{+0.08}_{-0.08}$	0.000008 $^{+0.000014}_{-0.000006}$	3.9 $^{+0.2}_{-0.2}$	1.11 $^{+0.07}_{-0.08}$	1.69 $^{+0.08}_{-0.07}$	16.33 $^{+0.06}_{-0.06}$	0.46 $^{+0.02}_{-0.02}$	0.96 $^{+0.03}_{-0.04}$	-1.2 $^{+0.1}_{-0.1}$
NGC 1851	61 $^{\dagger}$	0.93 $^{+0.02}_{-0.02}$	0.32 $^{+0.01}_{-0.01}$	5 $^{\dagger}$	1.96 $^{+0.02}_{-0.02}$	0.00002 $^{+0.00002}_{-0.00001}$	3.3 $^{+0.2}_{-0.2}$	0.76 $^{+0.05}_{-0.05}$	2.18 $^{+0.05}_{-0.05}$	12.39 $^{+0.07}_{-0.08}$	0.43 $^{+0.01}_{-0.01}$	0.96 $^{+0.03}_{-0.05}$	-2 $^{\dagger}$
NGC 2808	49 $^{\dagger}$	2.02 $^{+0.02}_{-0.03}$	0.48 $^{+0.01}_{-0.01}$	1.8 $^{+0.2}_{-0.3}$	2.00 $^{+0.02}_{-0.02}$	0.000022 $^{+0.000011}_{-0.000006}$	4.82 $^{+0.05}_{-0.05}$	0.37 $^{+0.02}_{-0.02}$	2.84 $^{+0.03}_{-0.03}$	10.36 $^{+0.05}_{-0.04}$	0.41 $^{+0.01}_{-0.01}$	0.95 $^{+0.04}_{-0.06}$	-0.2 $^{+0.2}_{-0.3}$
NGC 4372	8 $^{\dagger}$	0.55 $^{+0.02}_{-0.02}$	0.39 $^{+0.04}_{-0.03}$	5 $^{\dagger}$	1.6 $^{+0.3}_{-0.2}$	7 $^{\dagger}$	1.43 $^{+0.12}_{-0.10}$	0.70 $^{+0.04}_{-0.04}$	1.24 $^{+0.10}_{-0.10}$	5.29 $^{+0.08}_{-0.08}$	0.20 $^{+0.08}_{-0.06}$	0.7 $^{+0.2}_{-0.2}$	-2 $^{\dagger}$
NGC 4590	49 $^{\dagger}$	0.288 $^{+0.008}_{-0.009}$	0.50 $^{+0.02}_{-0.02}$	0.9 $^{+0.3}_{-0.3}$	1.7 $^{+0.2}_{-0.2}$	0.002 $^{+0.201}_{-0.002}$	2.2 $^{+0.2}_{-0.2}$	1.26 $^{+0.04}_{-0.04}$	1.61 $^{+0.08}_{-0.06}$	10.30 $^{+0.07}_{-0.09}$	0.44 $^{+0.03}_{-0.03}$	0.93 $^{+0.05}_{-0.04}$	-0.2 $^{+0.2}_{-0.4}$
NGC 4833	31 $^{\dagger}$	0.83 $^{+0.02}_{-0.02}$	0.45 $^{+0.03}_{-0.03}$	0.7 $^{+0.2}_{-0.2}$	0.8 $^{+0.1}_{-0.1}$	6 $^{\dagger}$	1.9 $^{+0.2}_{-0.1}$	0.81 $^{+0.04}_{-0.03}$	1.42 $^{+0.06}_{-0.07}$	6.47 $^{+0.05}_{-0.05}$	0.32 $^{+0.01}_{-0.02}$	0.97 $^{+0.02}_{-0.04}$	-0.7 $^{+0.2}_{-0.1}$
NGC 5024	9.9 $^{+0.3}_{-0.4}$	1.21 $^{+0.03}_{-0.03}$	1.02 $^{+0.08}_{-0.06}$	6 $^{\dagger}$	2.0 $^{+0.1}_{-0.1}$	0.00077 $^{+0.0021}_{-0.0006}$	3.0 $^{+0.2}_{-0.2}$	0.94 $^{+0.08}_{-0.07}$	1.87 $^{+0.07}_{-0.08}$	18.9 $^{+0.1}_{-0.1}$	0.110 $^{+0.009}_{-0.007}$	0.98 $^{+0.01}_{-0.03}$	-0.3 $^{+1.9}_{-2.3}$
NGC 5139	12.6 $^{+0.4}_{-0.6}$	6.81 $^{+0.04}_{-0.05}$	1.25 $^{+0.02}_{-0.02}$	0.89 $^{+0.04}_{-0.06}$	1.92 $^{+0.03}_{-0.02}$	0.0004 $^{+0.0001}_{-0.0001}$	4.97 $^{+0.02}_{-0.03}$	0.68 $^{+0.03}_{-0.03}$	1.53 $^{+0.01}_{-0.02}$	5.364 $^{+0.010}_{-0.007}$	0.44 $^{+0.02}_{-0.02}$	0.85 $^{+0.04}_{-0.05}$	0.20 $^{+0.03}_{-0.03}$
NGC 5272	10.7 $_{-0.5}^{+0.9}$	1.24 $^{+0.02}_{-0.02}$	0.46 $^{+0.01}_{-0.01}$	6 $^{\dagger}$	1.64 $^{+0.04}_{-0.04}$	0.000011 $^{+0.000038}_{-0.000008}$	2.3 $^{+0.1}_{-0.1}$	1.15 $^{+0.04}_{-0.04}$	1.41 $^{+0.05}_{-0.05}$	10.27 $^{+0.06}_{-0.06}$	0.115 $^{+0.013}_{-0.009}$	0.94 $^{+0.04}_{-0.07}$	0.3 $^{+1.9}_{-2.2}$
NGC 5904	23 $^{\dagger}$	1.17 $^{+0.03}_{-0.03}$	0.196 $^{+0.009}_{-0.009}$	5 $^{\dagger}$	1.58 $^{+0.06}_{-0.06}$	0.005 $^{+0.011}_{-0.003}$	4.8 $^{+0.2}_{-0.2}$	0.66 $^{+0.05}_{-0.05}$	1.00 $^{+0.05}_{-0.06}$	7.33 $^{+0.05}_{-0.05}$	0.27 $^{+0.01}_{-0.02}$	0.98 $^{+0.01}_{-0.03}$	-1.0 $^{+2.1}_{-2.3}$
NGC 5986 $^{\dagger}$	13 $^{\dagger}$	1.06 $^{+0.03}_{-0.03}$	0.71 $^{+0.07}_{-0.06}$	0.6 $^{+0.8}_{-0.3}$	2.0 $^{+0.2}_{-0.1}$	0.00010 $^{+0.00010}_{-0.00007}$	4.4 $^{+0.3}_{-0.4}$	1.20 $^{+0.06}_{-0.06}$	1.78 $^{+0.09}_{-0.11}$	10.45 $^{+0.08}_{-0.04}$	0.29 $^{+0.05}_{-0.04}$	0.96 $^{+0.03}_{-0.06}$	-0.7 $^{+0.8}_{-1.4}$
NGC 6093 $^{\dagger}$	22 $^{\dagger}$	1.28 $^{+0.04}_{-0.04}$	0.056 $^{+0.005}_{-0.004}$	3 $^{\dagger}$	1.37 $^{+0.05}_{-0.04}$	0.009 $^{+0.003}_{-0.003}$	4.5 $^{+0.4}_{-0.4}$	0.76 $^{+0.07}_{-0.06}$	2.01 $^{+0.07}_{-0.07}$	9.92 $^{+0.07}_{-0.07}$	0.493 $^{+0.005}_{-0.002}$	0.3 $^{+0.1}_{-0.1}$	-0.7 $^{+1.4}_{-2.0}$
NGC 6121 $^{\dagger}$	13.7 $_{-1.0}^{+0.9}$	0.76 $^{+0.01}_{-0.01}$	1.7 $^{+0.2}_{-0.2}$	5 $^{\dagger}$	1.0 $^{+0.1}_{-0.1}$	0.00002 $^{+0.00006}_{-0.00001}$	1.7 $^{+0.1}_{-0.1}$	0.95 $^{+0.08}_{-0.08}$	1.70 $^{+0.09}_{-0.10}$	1.83 $^{+0.01}_{-0.01}$	0.15 $^{+0.01}_{-0.01}$	0.97 $^{+0.02}_{-0.04}$	-1 $^{\dagger}$
NGC 6171	23 $^{\dagger}$	0.437 $^{+0.010}_{-0.008}$	0.88 $^{+0.07}_{-0.07}$	5 $^{\dagger}$	0.8 $^{+0.1}_{-0.1}$	0.004 $^{+0.002}_{-0.002}$	2.3 $^{+0.2}_{-0.1}$	1.12 $^{+0.04}_{-0.06}$	1.20 $^{+0.07}_{-0.05}$	5.48 $^{+0.05}_{-0.06}$	0.28 $^{+0.02}_{-0.02}$	0.98 $^{+0.02}_{-0.03}$	-0.8 $^{+1.5}_{-2.3}$
NGC 6205	24 $^{\dagger}$	1.42 $^{+0.03}_{-0.03}$	0.164 $^{+0.011}_{-0.010}$	2.8 $^{+1.2}_{-0.9}$	2.55 $^{+0.04}_{-0.03}$	0.00002 $^{+0.00003}_{-0.00001}$	2.8 $^{+0.3}_{-0.3}$	0.56 $^{+0.08}_{-0.09}$	1.39 $^{+0.07}_{-0.07}$	7.38 $^{+0.03}_{-0.04}$	0.43 $^{+0.04}_{-0.04}$	0.7 $^{+0.1}_{-0.2}$	-0.7 $^{+1.1}_{-1.3}$
NGC 6218	38 $_{-11}^{+11}$	0.46 $^{+0.01}_{-0.01}$	0.180 $^{+0.010}_{-0.009}$	4 $^{\dagger}$	0.78 $^{+0.07}_{-0.07}$	0.00009 $^{+0.00024}_{-0.00007}$	3.0 $^{+0.3}_{-0.3}$	0.62 $^{+0.06}_{-0.06}$	1.36 $^{+0.07}_{-0.06}$	5.09 $^{+0.03}_{-0.06}$	0.495 $^{+0.004}_{-0.009}$	0.57 $^{+0.12}_{-0.07}$	-1 $^{\dagger}$
NGC 6254	32 $^{\dagger}$	0.73 $^{+0.02}_{-0.02}$	0.25 $^{+0.01}_{-0.01}$	5 $^{\dagger}$	0.99 $^{+0.07}_{-0.08}$	0.0003 $^{+0.0003}_{-0.0002}$	2.9 $^{+0.2}_{-0.2}$	0.69 $^{+0.04}_{-0.04}$	1.31 $^{+0.06}_{-0.06}$	5.06 $^{+0.04}_{-0.04}$	0.32 $^{+0.02}_{-0.02}$	0.95 $^{+0.03}_{-0.07}$	-1 $^{\dagger}$
NGC 6266*	57 $^{\dagger}$	2.43 $^{+0.07}_{-0.05}$	0.089 $^{+0.011}_{-0.008}$	1.6 $^{+3.1}_{-0.5}$	1.10 $^{+0.07}_{-0.08}$	0.24 $^{+0.03}_{-0.02}$	3.0 $^{+0.3}_{-0.3}$	0.05 $^{+0.16}_{-0.18}$	1.92 $^{+0.08}_{-0.08}$	6.36 $^{+0.04}_{-0.04}$	0.48 $^{+0.02}_{-0.03}$	0.97 $^{+0.02}_{-0.03}$	-1.2 $^{+0.8}_{-0.5}$
NGC 6341	23 $^{\dagger}$	0.92 $^{+0.03}_{-0.03}$	0.23 $^{+0.01}_{-0.01}$	1.8 $^{+0.9}_{-0.8}$	1.73 $^{+0.07}_{-0.08}$	0.00006 $^{+0.00008}_{-0.00003}$	4.0 $^{+0.2}_{-0.2}$	1.06 $^{+0.05}_{-0.05}$	1.51 $^{+0.07}_{-0.07}$	8.35 $^{+0.04}_{-0.04}$	0.36 $^{+0.03}_{-0.04}$	0.97 $^{+0.02}_{-0.04}$	-0.9 $^{+0.9}_{-1.1}$
NGC 6352	26 $^{\dagger}$	0.32 $^{+0.01}_{-0.01}$	0.51 $^{+0.05}_{-0.04}$	6 $^{\dagger}$	0.04 $^{+0.06}_{-0.05}$	0.28 $^{+0.06}_{-0.05}$	2.9 $^{+0.3}_{-0.2}$	0.74 $^{+0.06}_{-0.06}$	0.82 $^{+0.07}_{-0.06}$	5.51 $^{+0.06}_{-0.06}$	0.229 $^{+0.008}_{-0.009}$	0.98 $^{+0.01}_{-0.03}$	-2 $^{\dagger}$
NGC 6362	10.8 $_{-5.2}^{+0.9}$	0.465 $^{+0.008}_{-0.028}$	0.37 $^{+0.30}_{-0.02}$	6.4 $^{+0.7}_{-3.3}$	1.93 $^{+0.08}_{-1.56}$	0.0004 $^{+0.00034}_{-0.0004}$	4.0 $^{+0.2}_{-2.0}$	0.647 $^{+0.156}_{-0.007}$	0.76 $^{+0.23}_{-0.02}$	7.56 $^{+0.08}_{-0.09}$	0.22 $^{+0.07}_{-0.06}$	0.81 $^{+0.16}_{-0.01}$	-0.7 $^{+0.9}_{-1.8}$
NGC 6366	10 $^{\dagger}$	0.262 $^{+0.010}_{-0.009}$	0.9 $^{+0.1}_{-0.1}$	5 $^{\dagger}$	2.1 $^{+0.5}_{-0.4}$	0.002 $^{+0.002}_{-0.001}$	1.7 $^{+0.1}_{-0.1}$	0.60 $^{+0.09}_{-0.10}$	1.1 $^{+0.1}_{-0.1}$	3.47 $^{+0.04}_{-0.04}$	0.36 $^{+0.08}_{-0.09}$	0.89 $^{+0.09}_{-0.18}$	-0.9 $^{+2.6}_{-2.7}$
NGC 6397*	63 $^{\dagger}$	0.417 $^{+0.007}_{-0.008}$	0.091 $^{+0.002}_{-0.002}$	5 $^{\dagger}$	1.51 $^{+0.04}_{-0.04}$	1.0 $^{+0.5}_{-0.4}$	2.8 $^{+0.2}_{-0.1}$	1.14 $^{+0.04}_{-0.04}$	1.29 $^{+0.04}_{-0.04}$	2.39 $^{+0.01}_{-0.01}$	0.4990 $^{+0.0007}_{-0.0020}$	0.98 $^{+0.01}_{-0.02}$	-0.8 $^{+2.1}_{-1.9}$
NGC 6541*	60 $^{\dagger}$	0.77 $^{+0.02}_{-0.02}$	0.186 $^{+0.008}_{-0.008}$	0.9 $^{+0.3}_{-0.2}$	1.15 $^{+0.08}_{-0.06}$	0.0004 $^{+0.0003}_{-0.0002}$	2.8 $^{+0.2}_{-0.2}$	0.84 $^{+0.05}_{-0.05}$	1.73 $^{+0.06}_{-0.06}$	7.32 $^{+0.05}_{-0.06}$	0.48 $^{+0.01}_{-0.02}$	0.95 $^{+0.04}_{-0.07}$	-1.5 $^{+0.2}_{-0.2}$
NGC 6681 $^{\dagger}$	50 $^{\dagger}$	0.60 $^{+0.02}_{-0.01}$	0.20 $^{+0.02}_{-0.02}$	1.1 $^{+0.1}_{-0.1}$	0.94 $^{+0.08}_{-0.08}$	0.03 $^{+0.02}_{-0.01}$	2.5 $^{+0.2}_{-0.2}$	1.06 $^{+0.03}_{-0.04}$	1.13 $^{+0.04}_{-0.03}$	9.17 $^{+0.09}_{-0.08}$	0.44 $^{+0.02}_{-0.02}$	0.989 $^{+0.008}_{-0.008}$	-1.5 $^{+0.2}_{-0.2}$
NGC 6723	20 $^{\dagger}$	0.73 $^{+0.01}_{-0.01}$	0.23 $^{+0.01}_{-0.01}$	0.08 $^{+0.10}_{-0.08}$	2.20 $^{+0.10}_{-0.11}$	0.005 $^{+0.004}_{-0.003}$	2.3 $^{+0.2}_{-0.2}$	0.75 $^{+0.08}_{-0.08}$	1.02 $^{+0.05}_{-0.06}$	8.00 $^{+0.04}_{-0.07}$	0.43 $^{+0.04}_{-0.04}$	0.86 $^{+0.09}_{-0.11}$	-1.0 $^{+0.1}_{-0.1}$
NGC 6752*	69 $^{\dagger}$	0.96 $^{+0.02}_{-0.02}$	0.062 $^{+0.004}_{-0.004}$	7.7 $^{+0.2}_{-0.4}$	1.63 $^{+0.04}_{-0.04}$	14.4 $^{+0.5}_{-0.8}$	4.2 $^{+0.2}_{-0.2}$	0.93 $^{+0.06}_{-0.06}$	1.04 $^{+0.05}_{-0.04}$	4.15 $^{+0.01}_{-0.01}$	0.495 $^{+0.004}_{-0.009}$	0.90 $^{+0.06}_{-0.08}$	2.0 $^{+0.6}_{-0.7}$
NGC 6779	39 $^{\dagger}$	0.541 $^{+0.009}_{-0.010}$	0.63 $^{+0.04}_{-0.04}$	6 $^{\dagger}$	0.96 $^{+0.08}_{-0.09}$	0.0006 $^{+0.0004}_{-0.0003}$	2.7 $^{+0.3}_{-0.3}$	0.93 $^{+0.04}_{-0.04}$	1.68 $^{+0.06}_{-0.06}$	10.49 $^{+0.07}_{-0.06}$	0.28 $^{+0.01}_{-0.02}$	0.90 $^{+0.08}_{-0.11}$	-0.8 $^{+2.1}_{-2.2}$
NGC 6809	3 $^{\dagger}$	0.74 $^{+0.03}_{-0.02}$	0.30 $^{+0.02}_{-0.02}$	5 $^{\dagger}$	2.3 $^{+0.2}_{-0.2}$	0.0001 $^{+0.0002}_{-0.0001}$	4.5 $^{+0.3}_{-0.3}$	0.81 $^{+0.06}_{-0.06}$	1.06 $^{+0.08}_{-0.08}$	5.31 $^{+0.04}_{-0.04}$	0.30 $^{+0.06}_{-0.05}$	0.91 $^{+0.07}_{-0.13}$	0.5 $^{+2.5}_{-2.8}$
NGC 7078*	25 $^{\dagger}$	1.64 $^{+0.03}_{-0.02}$	0.24 $^{+0.01}_{-0.01}$	1.4 $^{+0.1}_{-0.1}$	1.32 $^{+0.06}_{-0.06}$	0.00006 $^{+0.00005}_{-0.00004}$	3.8 $^{+0.3}_{-0.3}$	0.82 $^{+0.06}_{-0.06}$	1.59 $^{+0.05}_{-0.05}$	10.67 $^{+0.06}_{-0.08}$	0.23 $^{+0.01}_{-0.02}$	0.88 $^{+0.07}_{-0.09}$	-0.4 $^{+0.1}_{-0.1}$
NGC 7089	38 $^{\dagger}$	1.75 $^{+0.04}_{-0.05}$	0.28 $^{+0.03}_{-0.02}$	5 $^{\dagger}$	2.12 $^{+0.08}_{-0.08}$	0.00004 $^{+0.00004}_{-0.00002}$	4.2 $^{+0.4}_{-0.4}$	0.3 $^{+0.2}_{-0.2}$	1.99 $^{+0.05}_{-0.09}$	11.63 $^{+0.07}_{-0.08}$	0.36 $^{+0.02}_{-0.03}$	0.94 $^{+0.05}_{-0.09}$	-2 $^{\dagger}$
NGC 7099*	47 $^{\dagger}$	0.526 $^{+0.007}_{-0.011}$	0.269 $^{+0.016}_{-0.005}$	1.15 $^{+0.09}_{-0.08}$	0.77 $^{+0.06}_{-0.06}$	0.2 $^{+0.2}_{-0.2}$	3.9 $^{+0.3}_{-0.3}$	1.00 $^{+0.04}_{-0.03}$	1.42 $^{+0.07}_{-0.04}$	8.50 $^{+0.10}_{-0.08}$	0.349 $^{+0.008}_{-0.007}$	0.993 $^{+0.005}_{-0.007}$	-1.30 $^{+0.14}_{-0.07}$

**Table A1.** Median and  $1\sigma$  uncertainties of the best-fitting model parameters, for all clusters in our sample. Note that the uncertainties presented here represent only the statistical uncertainties, and likely underestimate the true errors. All clusters classified as core-collapsed in S. C. Trager et al. (1995) are denoted by an asterisk. All clusters with  $R'_G < 1.5$  kpc are denoted by a dagger.

Cluster	Initial Conditions			Present Day Conditions			
	$\log_{10}(\rho_{h,0})$	$f_{\text{BH},0}$	$v_{\text{esc},0}$	$\log_{10}(\rho_h)$	$f_{\text{BH}}$	$M$	$r_h$
	$[M_{\odot} \text{ pc}^{-3}]$	[%]	[km/s]	$[M_{\odot} \text{ pc}^{-3}]$	[%]	$[10^6 M_{\odot}]$	[pc]
NGC 104	6.01 <sup>+0.14</sup> <sub>-0.07</sub>	5.44 <sup>+0.15</sup> <sub>-0.08</sub>	196 <sup>+13</sup> <sub>-7</sub>	2.78 <sup>+0.02</sup> <sub>-0.01</sub>	1.23 <sup>+0.03</sup> <sub>-0.02</sub>	0.810 <sup>+0.007</sup> <sub>-0.006</sub>	5.45 <sup>+0.04</sup> <sub>-0.05</sub>
NGC 362 <sup>†*</sup>	6.94 <sup>+0.07</sup> <sub>-0.07</sub>	7.07 <sup>+0.07</sup> <sub>-0.08</sub>	225 <sup>+7</sup> <sub>-8</sub>	2.96 <sup>+0.02</sup> <sub>-0.02</sub>	0.30 <sup>+0.01</sup> <sub>-0.02</sub>	0.297 <sup>+0.005</sup> <sub>-0.004</sub>	3.40 <sup>+0.04</sup> <sub>-0.05</sub>
NGC 1261	5.87 <sup>+0.07</sup> <sub>-0.07</sub>	6.41 <sup>+0.08</sup> <sub>-0.09</sub>	122 <sup>+4</sup> <sub>-4</sub>	2.25 <sup>+0.01</sup> <sub>-0.01</sub>	0.30 <sup>+0.02</sup> <sub>-0.02</sub>	0.188 <sup>+0.003</sup> <sub>-0.003</sub>	5.03 <sup>+0.05</sup> <sub>-0.05</sub>
NGC 1851	6.54 <sup>+0.06</sup> <sub>-0.06</sub>	6.20 <sup>+0.07</sup> <sub>-0.07</sub>	190 <sup>+5</sup> <sub>-5</sub>	2.97 <sup>+0.01</sup> <sub>-0.01</sub>	0.21 <sup>+0.01</sup> <sub>-0.01</sub>	0.329 <sup>+0.004</sup> <sub>-0.004</sub>	3.49 <sup>+0.03</sup> <sub>-0.03</sub>
NGC 2808	6.34 <sup>+0.04</sup> <sub>-0.04</sub>	5.58 <sup>+0.05</sup> <sub>-0.04</sub>	227 <sup>+4</sup> <sub>-4</sub>	3.331 <sup>+0.010</sup> <sub>-0.007</sub>	0.461 <sup>+0.008</sup> <sub>-0.009</sub>	0.931 <sup>+0.008</sup> <sub>-0.010</sub>	3.73 <sup>+0.01</sup> <sub>-0.02</sub>
NGC 3201	6.7 <sup>+0.2</sup> <sub>-0.1</sub>	7.9 <sup>+0.2</sup> <sub>-0.1</sub>	158 <sup>+11</sup> <sub>-9</sub>	1.79 <sup>+0.03</sup> <sub>-0.03</sub>	0.37 <sup>+0.03</sup> <sub>-0.04</sub>	0.142 <sup>+0.003</sup> <sub>-0.003</sub>	6.5 <sup>+0.2</sup> <sub>-0.2</sub>
NGC 4372	6.0 <sup>+0.1</sup> <sub>-0.1</sub>	7.8 <sup>+0.2</sup> <sub>-0.2</sub>	131 <sup>+8</sup> <sub>-8</sub>	1.67 <sup>+0.02</sup> <sub>-0.02</sub>	1.2 <sup>+0.1</sup> <sub>-0.1</sub>	0.163 <sup>+0.005</sup> <sub>-0.005</sub>	7.4 <sup>+0.1</sup> <sub>-0.1</sub>
NGC 4590	5.44 <sup>+0.07</sup> <sub>-0.06</sub>	6.56 <sup>+0.08</sup> <sub>-0.08</sub>	84 <sup>+3</sup> <sub>-3</sub>	1.61 <sup>+0.02</sup> <sub>-0.02</sub>	0.20 <sup>+0.02</sup> <sub>-0.02</sub>	0.116 <sup>+0.003</sup> <sub>-0.003</sub>	7.0 <sup>+0.1</sup> <sub>-0.1</sub>
NGC 4833	6.05 <sup>+0.10</sup> <sub>-0.08</sub>	7.57 <sup>+0.13</sup> <sub>-0.08</sub>	151 <sup>+8</sup> <sub>-5</sub>	2.37 <sup>+0.01</sup> <sub>-0.01</sub>	1.09 <sup>+0.05</sup> <sub>-0.06</sub>	0.188 <sup>+0.004</sup> <sub>-0.003</sub>	4.58 <sup>+0.05</sup> <sub>-0.05</sub>
NGC 5024	5.14 <sup>+0.09</sup> <sub>-0.10</sub>	6.7 <sup>+0.1</sup> <sub>-0.1</sub>	121 <sup>+5</sup> <sub>-5</sub>	1.82 <sup>+0.02</sup> <sub>-0.01</sub>	2.8 <sup>+0.1</sup> <sub>-0.1</sub>	0.55 <sup>+0.01</sup> <sub>-0.01</sub>	9.9 <sup>+0.2</sup> <sub>-0.1</sub>
NGC 5139	5.62 <sup>+0.02</sup> <sub>-0.02</sub>	7.85 <sup>+0.03</sup> <sub>-0.03</sub>	259 <sup>+2</sup> <sub>-2</sub>	2.608 <sup>+0.003</sup> <sub>-0.002</sub>	8.31 <sup>+0.06</sup> <sub>-0.06</sub>	3.02 <sup>+0.01</sup> <sub>-0.01</sub>	9.62 <sup>+0.03</sup> <sub>-0.02</sub>
NGC 5272	6.19 <sup>+0.05</sup> <sub>-0.04</sub>	7.30 <sup>+0.07</sup> <sub>-0.06</sub>	183 <sup>+4</sup> <sub>-4</sub>	2.21 <sup>+0.01</sup> <sub>-0.01</sub>	1.54 <sup>+0.08</sup> <sub>-0.07</sub>	0.507 <sup>+0.007</sup> <sub>-0.008</sub>	7.18 <sup>+0.09</sup> <sub>-0.08</sub>
NGC 5904	7.27 <sup>+0.07</sup> <sub>-0.07</sub>	8.26 <sup>+0.07</sup> <sub>-0.08</sub>	271 <sup>+9</sup> <sub>-9</sub>	2.28 <sup>+0.02</sup> <sub>-0.02</sub>	1.22 <sup>+0.07</sup> <sub>-0.07</sub>	0.369 <sup>+0.007</sup> <sub>-0.007</sub>	6.13 <sup>+0.09</sup> <sub>-0.09</sub>
NGC 5986 <sup>†</sup>	5.5 <sup>+0.1</sup> <sub>-0.1</sub>	6.6 <sup>+0.2</sup> <sub>-0.1</sub>	135 <sup>+9</sup> <sub>-7</sub>	2.72 <sup>+0.02</sup> <sub>-0.02</sub>	0.86 <sup>+0.10</sup> <sub>-0.10</sub>	0.284 <sup>+0.007</sup> <sub>-0.006</sub>	4.02 <sup>+0.06</sup> <sub>-0.06</sub>
NGC 6093 <sup>†</sup>	8.9 <sup>+0.1</sup> <sub>-0.1</sub>	7.60 <sup>+0.05</sup> <sub>-0.05</sub>	530 <sup>+30</sup> <sub>-30</sub>	3.385 <sup>+0.010</sup> <sub>-0.009</sub>	0.029 <sup>+0.003</sup> <sub>-0.002</sub>	0.292 <sup>+0.005</sup> <sub>-0.004</sub>	2.43 <sup>+0.02</sup> <sub>-0.01</sub>
NGC 6121 <sup>†</sup>	4.3 <sup>+0.1</sup> <sub>-0.1</sub>	5.97 <sup>+0.09</sup> <sub>-0.11</sub>	74 <sup>+3</sup> <sub>-4</sub>	2.33 <sup>+0.01</sup> <sub>-0.01</sub>	3.5 <sup>+0.2</sup> <sub>-0.2</sub>	0.084 <sup>+0.002</sup> <sub>-0.001</sub>	3.62 <sup>+0.05</sup> <sub>-0.04</sub>
NGC 6171	4.9 <sup>+0.1</sup> <sub>-0.1</sub>	6.11 <sup>+0.08</sup> <sub>-0.08</sub>	78 <sup>+4</sup> <sub>-3</sub>	2.21 <sup>+0.02</sup> <sub>-0.02</sub>	0.86 <sup>+0.08</sup> <sub>-0.07</sub>	0.057 <sup>+0.001</sup> <sub>-0.001</sub>	3.47 <sup>+0.05</sup> <sub>-0.04</sub>
NGC 6205	7.59 <sup>+0.09</sup> <sub>-0.10</sub>	8.27 <sup>+0.11</sup> <sub>-0.10</sub>	330 <sup>+10</sup> <sub>-10</sub>	2.741 <sup>+0.009</sup> <sub>-0.009</sub>	0.72 <sup>+0.04</sup> <sub>-0.03</sub>	0.436 <sup>+0.005</sup> <sub>-0.006</sub>	4.55 <sup>+0.04</sup> <sub>-0.03</sub>
NGC 6218	6.98 <sup>+0.07</sup> <sub>-0.09</sub>	7.61 <sup>+0.08</sup> <sub>-0.10</sub>	178 <sup>+7</sup> <sub>-8</sub>	2.297 <sup>+0.010</sup> <sub>-0.010</sub>	0.162 <sup>+0.013</sup> <sub>-0.009</sub>	0.098 <sup>+0.003</sup> <sub>-0.002</sub>	3.88 <sup>+0.05</sup> <sub>-0.03</sub>
NGC 6254	6.72 <sup>+0.08</sup> <sub>-0.07</sub>	7.80 <sup>+0.10</sup> <sub>-0.08</sub>	187 <sup>+7</sup> <sub>-6</sub>	2.25 <sup>+0.02</sup> <sub>-0.02</sub>	0.63 <sup>+0.06</sup> <sub>-0.05</sub>	0.205 <sup>+0.004</sup> <sub>-0.004</sub>	5.16 <sup>+0.08</sup> <sub>-0.10</sub>
NGC 6266 <sup>†*</sup>	8.6 <sup>+0.1</sup> <sub>-0.2</sub>	7.51 <sup>+0.04</sup> <sub>-0.04</sub>	580 <sup>+30</sup> <sub>-40</sub>	3.50 <sup>+0.01</sup> <sub>-0.02</sub>	0.25 <sup>+0.04</sup> <sub>-0.02</sub>	0.69 <sup>+0.02</sup> <sub>-0.01</sub>	2.95 <sup>+0.06</sup> <sub>-0.03</sub>
NGC 6341	6.96 <sup>+0.10</sup> <sub>-0.10</sub>	7.7 <sup>+0.1</sup> <sub>-0.1</sub>	220 <sup>+10</sup> <sub>-10</sub>	2.67 <sup>+0.02</sup> <sub>-0.02</sub>	0.31 <sup>+0.03</sup> <sub>-0.02</sub>	0.294 <sup>+0.006</sup> <sub>-0.006</sub>	4.22 <sup>+0.08</sup> <sub>-0.07</sub>
NGC 6352	5.5 <sup>+0.1</sup> <sub>-0.1</sub>	5.97 <sup>+0.09</sup> <sub>-0.09</sub>	89 <sup>+6</sup> <sub>-5</sub>	1.70 <sup>+0.02</sup> <sub>-0.02</sub>	1.10 <sup>+0.08</sup> <sub>-0.08</sub>	0.061 <sup>+0.002</sup> <sub>-0.002</sub>	5.26 <sup>+0.08</sup> <sub>-0.08</sub>
NGC 6362	6.06 <sup>+0.06</sup> <sub>-0.81</sub>	6.96 <sup>+0.04</sup> <sub>-0.46</sub>	125 <sup>+3</sup> <sub>-35</sub>	1.71 <sup>+0.01</sup> <sub>-0.18</sub>	1.29 <sup>+0.89</sup> <sub>-0.02</sub>	0.097 <sup>+0.003</sup> <sub>-0.002</sub>	6.06 <sup>+1.00</sup> <sub>-0.04</sub>
NGC 6366	4.7 <sup>+0.2</sup> <sub>-0.2</sub>	5.6 <sup>+0.1</sup> <sub>-0.1</sub>	61 <sup>+5</sup> <sub>-5</sub>	1.72 <sup>+0.02</sup> <sub>-0.02</sub>	1.3 <sup>+0.1</sup> <sub>-0.1</sub>	0.033 <sup>+0.001</sup> <sub>-0.001</sub>	4.23 <sup>+0.06</sup> <sub>-0.07</sub>
NGC 6397 <sup>*</sup>	6.1 <sup>+0.1</sup> <sub>-0.1</sub>	7.73 <sup>+0.12</sup> <sub>-0.10</sub>	127 <sup>+8</sup> <sub>-6</sub>	1.84 <sup>+0.03</sup> <sub>-0.03</sub>	0.44 <sup>+0.04</sup> <sub>-0.03</sub>	0.115 <sup>+0.002</sup> <sub>-0.002</sub>	5.8 <sup>+0.1</sup> <sub>-0.1</sub>
NGC 6541 <sup>*</sup>	7.16 <sup>+0.07</sup> <sub>-0.06</sub>	7.55 <sup>+0.08</sup> <sub>-0.09</sub>	226 <sup>+8</sup> <sub>-6</sub>	2.77 <sup>+0.01</sup> <sub>-0.01</sub>	0.160 <sup>+0.011</sup> <sub>-0.009</sub>	0.226 <sup>+0.003</sup> <sub>-0.003</sub>	3.59 <sup>+0.04</sup> <sub>-0.04</sub>
NGC 6681 <sup>†</sup>	6.9 <sup>+0.1</sup> <sub>-0.1</sub>	7.87 <sup>+0.09</sup> <sub>-0.08</sub>	189 <sup>+12</sup> <sub>-10</sub>	2.86 <sup>+0.02</sup> <sub>-0.02</sub>	0.15 <sup>+0.02</sup> <sub>-0.01</sub>	0.089 <sup>+0.002</sup> <sub>-0.002</sub>	2.45 <sup>+0.04</sup> <sub>-0.03</sub>
NGC 6723	6.86 <sup>+0.06</sup> <sub>-0.07</sub>	7.36 <sup>+0.05</sup> <sub>-0.06</sub>	198 <sup>+6</sup> <sub>-6</sub>	2.29 <sup>+0.02</sup> <sub>-0.01</sub>	0.65 <sup>+0.03</sup> <sub>-0.04</sub>	0.169 <sup>+0.003</sup> <sub>-0.003</sub>	4.70 <sup>+0.05</sup> <sub>-0.09</sub>
NGC 6752 <sup>*</sup>	8.69 <sup>+0.09</sup> <sub>-0.07</sub>	8.60 <sup>+0.03</sup> <sub>-0.03</sub>	440 <sup>+20</sup> <sub>-10</sub>	2.70 <sup>+0.01</sup> <sub>-0.01</sub>	0.124 <sup>+0.012</sup> <sub>-0.010</sub>	0.226 <sup>+0.003</sup> <sub>-0.003</sub>	3.77 <sup>+0.04</sup> <sub>-0.04</sub>
NGC 6779	5.41 <sup>+0.10</sup> <sub>-0.09</sub>	6.93 <sup>+0.09</sup> <sub>-0.09</sub>	103 <sup>+4</sup> <sub>-4</sub>	2.03 <sup>+0.02</sup> <sub>-0.02</sub>	0.72 <sup>+0.05</sup> <sub>-0.05</sub>	0.151 <sup>+0.002</sup> <sub>-0.002</sub>	5.54 <sup>+0.07</sup> <sub>-0.07</sub>
NGC 6809	6.5 <sup>+0.1</sup> <sub>-0.1</sub>	8.2 <sup>+0.1</sup> <sub>-0.1</sub>	173 <sup>+9</sup> <sub>-9</sub>	2.05 <sup>+0.01</sup> <sub>-0.01</sub>	1.12 <sup>+0.07</sup> <sub>-0.06</sub>	0.184 <sup>+0.005</sup> <sub>-0.005</sub>	5.83 <sup>+0.06</sup> <sub>-0.05</sub>
NGC 7078 <sup>*</sup>	7.15 <sup>+0.08</sup> <sub>-0.08</sub>	7.99 <sup>+0.11</sup> <sub>-0.09</sub>	290 <sup>+11</sup> <sub>-9</sub>	2.710 <sup>+0.010</sup> <sub>-0.012</sub>	0.84 <sup>+0.03</sup> <sub>-0.03</sub>	0.620 <sup>+0.007</sup> <sub>-0.008</sub>	5.25 <sup>+0.04</sup> <sub>-0.05</sub>
NGC 7089	7.0 <sup>+0.1</sup> <sub>-0.1</sub>	7.6 <sup>+0.2</sup> <sub>-0.2</sub>	280 <sup>+20</sup> <sub>-20</sub>	2.90 <sup>+0.03</sup> <sub>-0.02</sub>	0.90 <sup>+0.07</sup> <sub>-0.09</sub>	0.61 <sup>+0.02</sup> <sub>-0.01</sub>	4.5 <sup>+0.1</sup> <sub>-0.1</sub>
NGC 7099 <sup>*</sup>	6.51 <sup>+0.03</sup> <sub>-0.09</sub>	7.51 <sup>+0.05</sup> <sub>-0.13</sub>	155 <sup>+3</sup> <sub>-6</sub>	2.336 <sup>+0.007</sup> <sub>-0.008</sub>	0.205 <sup>+0.006</sup> <sub>-0.013</sub>	0.140 <sup>+0.002</sup> <sub>-0.002</sub>	4.25 <sup>+0.04</sup> <sub>-0.03</sub>

**Table A2.** Median and  $1\sigma$  uncertainties of certain derived quantities (i.e. parameters not directly varied during fitting) of the best-fitting models, for all clusters in our sample. These include the initial half-mass density, BH mass fraction and central escape velocity, and the present-day half-mass density, BH mass fraction, total cluster mass and half-mass radius. The initial mass and radius values are listed in Table A1. Note that the uncertainties presented here represent only the statistical uncertainties, and likely underestimate the true errors. All clusters classified as core-collapsed in *S. C. Trager et al. (1995)* are denoted by an asterisk. All clusters with  $R'_G < 1.5$  kpc are denoted by a dagger.

simulations adopting a non-canonical IMF, and to re-examine which models best match all of the given data, and what impacts this would have on studies which use these models to represent MW clusters.